PAPER

MARS-Q modeling of kink-peeling instabilities in DIII-D QH-mode plasma

IOP Publishing | International Atomic Energy Agency Nuclear Fusion

Nucl. Fusion **61** (2021) 046038 (23pp) https://doi.org/10.1088/1741-4326/abe7bc

MARS-Q modeling of kink-peeling instabilities in DIII-D QH-mode plasma

G.Q. Dong[1,*], Y.Q. Liu[2,*], X. Chen[2], G.Z. Hao[1], Y. Liu[1], S. Wang[1], N. Zhang[1] and G.L. Xia[3]

[1] Southwestern Institute of Physics, P.O. Box 432, Chengdu 610041, China
[2] General Atomics, P.O. Box 85608, San Diego, CA 92186-5608, United States of America
[3] CCFE, Culham Science Centre, Abingdon, OX14 3DB, United Kingdom of Great Britain and Northern Ireland

E-mail: donggq@swip.ac.cn and liuy@fusion.gat.com

Received 22 December 2020, revised 4 February 2021
Accepted for publication 18 February 2021
Published 22 March 2021

Abstract

In quiescent H-mode (QH-mode) regime, edge harmonic oscillations (EHOs) are believed to provide necessary radial transport to prevent occurrence of large edge localized modes. A systematic modeling study is performed here on the low-n EHOs in a DIII-D QH-mode plasma (Chen *et al* 2016 *Nucl. Fusion* **56** 076011), by utilizing the MARS-Q code (Liu *et al* 2013 *Phys. Plasmas* **20** 042503). Both the $n = 1$ and $n = 2$ instabilities are found to be strongly localized near the plasma edge, exhibiting the edge-peeling characteristics. The DIII-D resistive wall is found to have minor effects on these instabilities. The plasma resistivity is found to strongly modify the mode growth rate. Assuming the Spitzer model for the plasma resistivity, the computed mode growth rate scales as $S^{-1/3}$ with S being the Lundquist number. Toroidal flow of the plasma slightly stabilizes these edge localized kink-peeling modes. Drift kinetic effects all have a destabilization effect on these modes. Non-perturbative magneto-hydrodynamic-kinetic hybrid computations find that the drift kinetic effects associated with thermal particle species push the peak location of the eigenmode radially inward but still in the pedestal region. The modeled plasma temperature and density fluctuations in the plasma edge region, as well as the poloidal magnetic field perturbations along both the low and high field sides of the plasma surface, are in good agreement with experimental measurements. Finally, the quasi-linear initial value simulations find a strong non-linear interplay between the kink-peeling instability and the toroidal flow near the plasma edge. The combined effect of the damping of the flow amplitude and change of the edge flow shear is found to be the stabilizing factor for the kink-peeling mode, leading to the mode saturation and thus EHOs.

Keywords: edge harmonic oscillations, drift kinetic effect, non-linear interplay

(Some figures may appear in colour only in the online journal)

1. Introduction

The quiescent H-mode (QH-mode) regime offers a promising tokamak plasma scenario with good energy confinement and without edge localized modes (ELMs) [1, 2]. The absence of ELMs avoids large pulsed particle and heat fluxes reaching the divertor surface. The QH-regime can thus be exploited as a highly beneficial operating scenario for next step tokamak devices. This regime has been accessed in several machines such as DIII-D [3, 4], ASDEX Upgrade [5], JET [5], and JT-60U [6, 7]. This type of ELM-free H-mode regime is often achieved at relatively low plasma density in experiments, and is found to be accompanied by the presence of edge harmonic oscillations (EHOs) [1, 4, 8, 9], which are believed to provide

* Authors to whom any correspondence should be addressed.

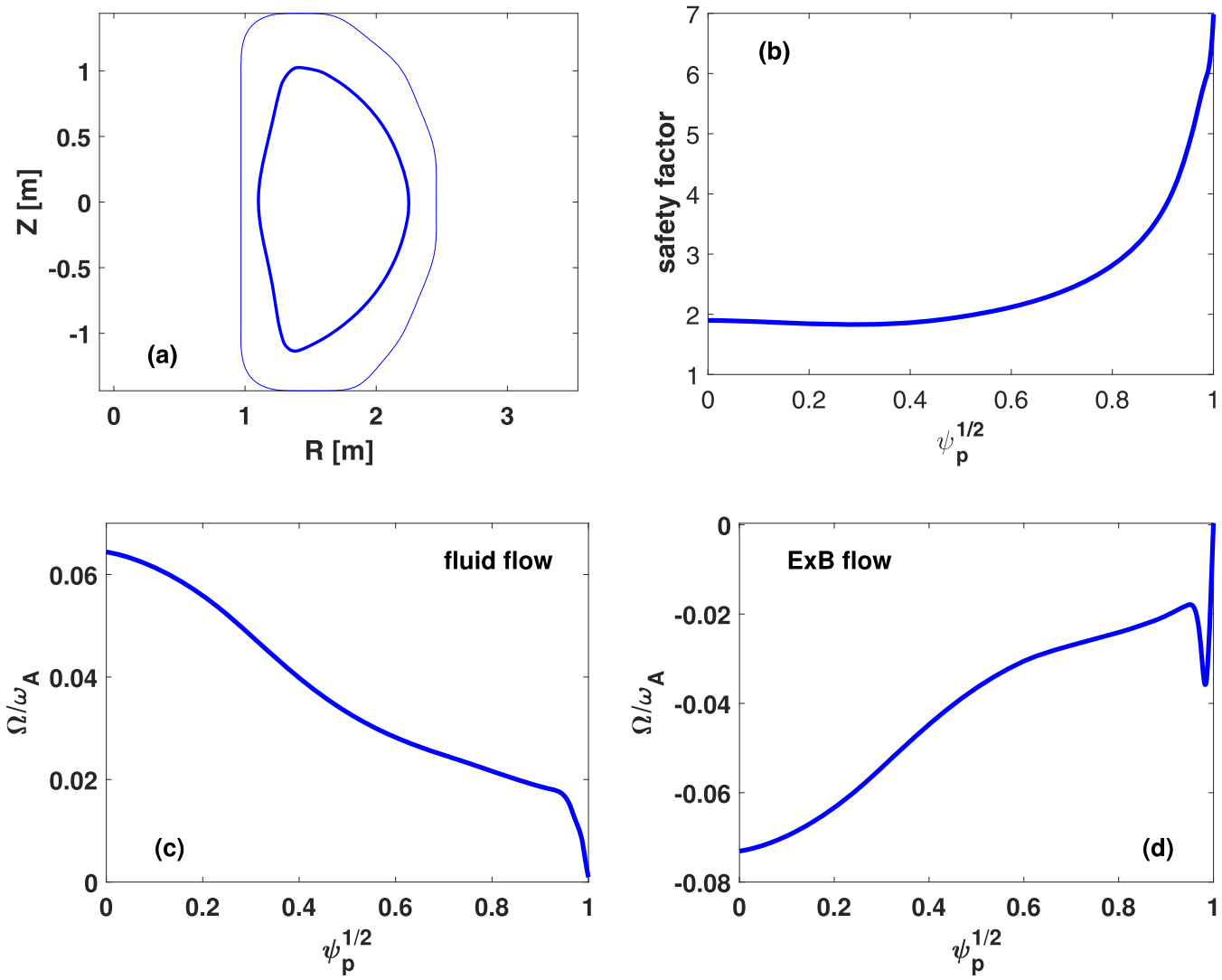

Figure 1. Shown are (*a*) the plasma boundary shape (thick line) and the resistive wall shape (thin line), and (*b*)–(*d*) the radial profiles of various equilibrium quantities re-constructed from the DIII-D discharge 157102 at 2420 ms: (*b*) the safety factor, (*c*) the toroidal fluid rotation frequency normalized by the Alfvén frequency, and (*d*) the $E \times B$ rotation frequency normalized by the Alfvén frequency. ψ_p denotes the normalized poloidal flux.

necessary radial transport to eliminate ELMs by the dynamic self-regularization of the plasma [1, 4].

The saturated kink-peeling mode has been suggested as a possible candidate for EHO [10–13]. According to this interpretation, an edge localized kink-peeling instability, with the dominant toroidal mode number being typically below 3 ($n \leqslant 3$), is non-linearly saturated by the plasma flow, thus leading to EHOs. Indeed, experimental results in DIII-D [12] have shown that access to the QH-regime with coherent EHOs requires fast plasma rotation and large flow shear in the pedestal region.

The detailed triggering and saturation mechanisms of EHOs have not been fully understood. Several possible physics scenarios have previously been suggested based on non-linear magneto-hydrodynamic (MHD) simulations. For instance, full-MHD modeling with the NIMROD code showed that flattening of the pressure and current profiles is a likely mechanism for eliminating the free-energy drive that leads to the mode saturation [14]. The JOREK simulations, based on a reduced MHD formulation, found an initial burst associated with high-n harmonics, followed by the non-linear saturation of the plasma into a new 3D stationary state dominated by low-n harmonics (the kink-peeling modes) [15]. Furthermore, the $E \times B$ flow was found to strongly stabilize the high-n modes but destabilize the low-n modes. All the aforementioned studies were carried out within the MHD model, without taking into account the possible drift kinetic effects from plasma particles. Direct interaction between the plasma flow and the kink-peeling mode was not emphasized in these studies either. These are the key physics that we wish to exploit in the present study, among other important aspects.

More specifically, we will perform a systematic numerical investigation of various physical effects on the kink-peeling instabilities, including the wall eddy current effect, the influence of the plasma resistivity, the kinetic effects associated with thermal particle drift motions, the effect of plasma

pedestal toroidal flow and flow shear, and finally the dynamics of self-consistent interaction between the plasma flow and the kink-peeling mode. We perform the study for a DIII-D QH-mode plasma from discharge 157102 [12]. The modeling tools that we utilize are the MARS-F/K/Q suite of codes [16–18]. Quantitative comparison will be made between modeling and experiments.

The paper is organized as follows. The computational model and the plasma equilibrium are introduced in section 2. Section 3 reports results of linear stability computations including various physics effects. Comparison between the modeled and the experimentally measured fluctuations in the magnetic field, the plasma density and temperature, is reported in section 4. Self-consistent non-linear interaction between the plasma flow and the kink-peeling instability is simulated in section 5. Section 6 summarizes and discusses the results.

2. Computational model and plasma equilibrium

In this work, the MARS-F/K/Q [16–18] suite of codes are utilized to study various physics aspects of EHOs. For simplicity, this suite of codes are also referred to as MARS-Q in this work, if not otherwise specified. Without drift kinetic effects, the code solves the single fluid perturbed MHD equations that incorporate a sheared equilibrium toroidal flow, with the angular frequency Ω being a function of the magnetic flux surface

$$\left(\frac{\partial}{\partial t}+in\Omega\right)\xi=\mathbf{v}+(\xi\cdot\nabla\Omega)R^2\nabla\phi \tag{1}$$

$$\rho\left(\frac{\partial}{\partial t}+in\Omega\right)\mathbf{v}=-\nabla p+\mathbf{j}\times\mathbf{B}+\mathbf{J}\times\mathbf{b}-\rho\left[2\Omega\nabla\hat{Z}\times\mathbf{v}+(\mathbf{v}\cdot\nabla\Omega)R^2\nabla\phi\right]-\nabla\cdot(\rho\xi)\Omega\hat{Z}\times\mathbf{V}_0 \tag{2}$$

$$\left(\frac{\partial}{\partial t}+in\Omega\right)\mathbf{b}=\nabla\times(\mathbf{v}\times\mathbf{B})+(\mathbf{b}\cdot\Omega)R^2\nabla\phi-\nabla\times(\eta\mathbf{j}) \tag{3}$$

$$\left(\frac{\partial}{\partial t}+in\Omega\right)p=-\mathbf{v}\cdot\nabla P-\Gamma P\nabla\cdot\mathbf{v} \tag{4}$$

$$\mathbf{j}=\nabla\times\mathbf{b}, \tag{5}$$

where R is the plasma major radius, ϕ the geometric toroidal angle of the torus, and $\hat{Z}$ the unit vector in the vertical direction on the poloidal plane. Variables ξ, $\mathbf{v}$, $\mathbf{b}$, p, and $\mathbf{j}$ denote the perturbed quantities for the plasma displacement, the fluid velocity, the magnetic field, the plasma pressure, and the plasma current, respectively. n is the toroidal harmonic number, which will be chosen as $n=1,2,3$ in the present study. The equilibrium plasma density, magnetic field, plasma current and pressure are denoted by ρ, $\mathbf{B}$, $\mathbf{J}$ and P, respectively. $\Gamma=5/3$ is the ratio of specific heats.

Note that the plasma displacement in MARS-Q is defined via the Lagrangian velocity in a rotating plasma, i.e. $\mathrm{d}\xi/\mathrm{d}t=\mathbf{v}_\mathrm{L}$. With a pure toroidal plasma flow, the convection part of the full time derivative contributes a Doppler shift term of $in\Omega$, which appears in the left-hand side of equations (1)–(4). The Lagrangian velocity, being expressed via the Eulerian counterpart as adopted in this work, yields the right-hand side of equation (1). The above MHD equations in the plasma domain are solved together with the perturbed magnetic field equations in the vacuum region, as well as a radial field diffusion equation associated with the resistive wall, with thin wall approximation [19].

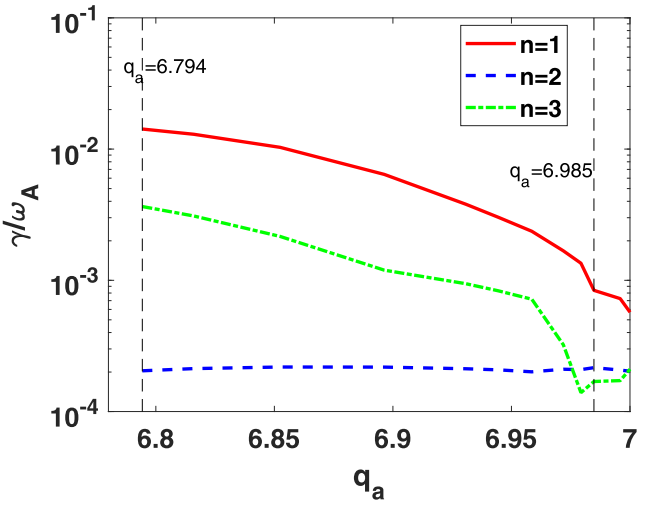

Figure 2. The MARS-F computed growth rate of the $n=1,2,3$ ideal instabilities while slightly smoothing the plasma boundary shape near the X-point of the plasma separatrix, resulting in variation of the edge safety factor q_a with q_{95} being nearly unchanged. No plasma equilibrium flow nor the presence of a resistive wall is assumed here. The two vertical dashed lines indicate the two equilibria that are extensively studied in this work.

The drift kinetic effects are incorporated via a non-perturbative MHD-kinetic hybrid formulation (MARS-K). An alternative way of viewing this hybrid scheme is to replace the single fluid, ideal gas closure by the drift kinetic closure, as has been rigorously derived for a toroidal plasma [20]. With the hybrid formulation, the perturbed scalar pressure from the above equations (1)–(4) is replaced by a perturbed pressure tensor $\mathbf{p}$ [21]

$$\mathbf{p}=p_\parallel\mathbf{bb}+p_\perp(\mathbf{I}-\mathbf{bb}), \tag{6}$$

$$p_g=p_g^\mathrm{a}+\alpha_\mathrm{D}p_g^\mathrm{D}+\alpha_\mathrm{B}p_g^\mathrm{B}+\alpha_\mathrm{C}p_g^\mathrm{C},\quad g=\parallel\ \text{or}\ \perp, \tag{7}$$

where $\mathbf{b}$ is the unit vector along the equilibrium magnetic field line and $\mathbf{I}$ the unit tensor. The subscript 'g' is introduced to denote either the parallel or the perpendicular (to the equilibrium magnetic field line) component of the perturbed pressure tensor. The perturbed pressure component p_g consists of an adiabatic contribution p_g^a and the non-adiabatic contributions due to drift kinetic resonances between plasma particles and the mode. The adiabatic contribution does not involve mode-particle resonances.

The non-adiabatic contributions generally come from various types of drift kinetic resonances, including the precessional drift resonance of trapped thermal particles (p_g^D), the bounce resonance of trapped particles (p_g^B) as well as the transit resonance of circulating particles (p_g^C). The essential piece of

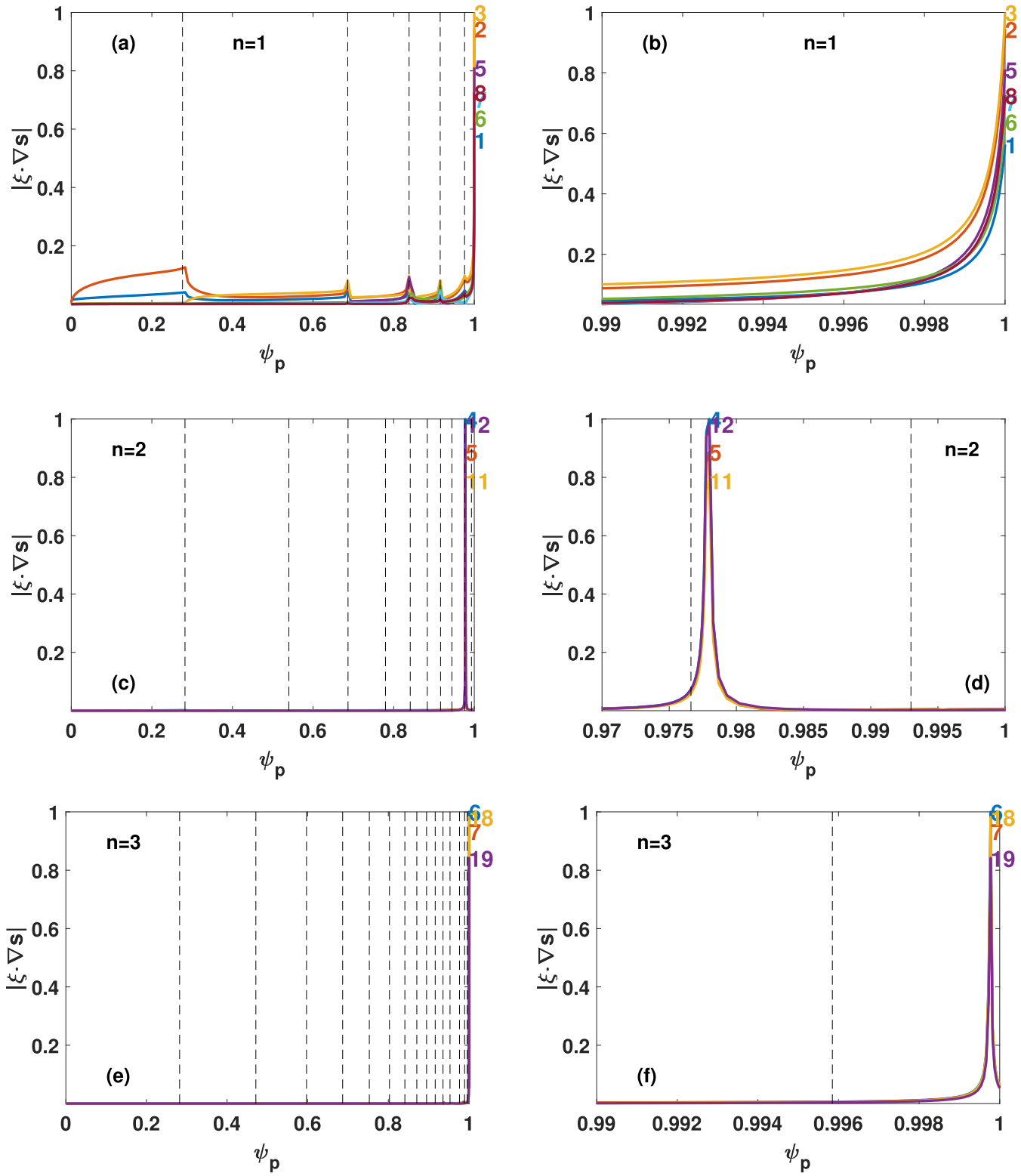

Figure 3. The MARS-F computed eigenfunctions, in terms of the poloidal Fourier harmonics of the radial displacement of the plasma, for the $n = 1$ (top panels), $n = 2$ (middle panels), and $n = 3$ (bottom panels) ideal instabilities, in the absence of the resistive wall and assuming vanishing plasma equilibrium flow. The right panels show the zoomed-in eigenmode structure near the plasma edge. The vertical dashed lines indicate the radial location of rational surfaces associated with the perturbation. Considered is an equilibrium with the edge safety factor $q_a = 6.985$.

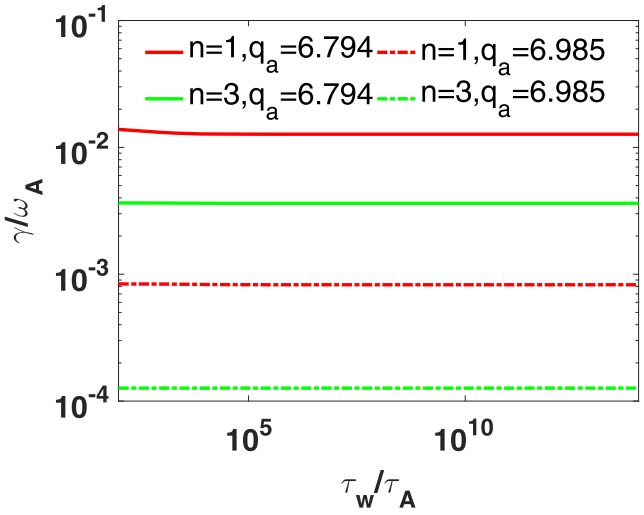

Figure 4. Effect of the wall time τ_w (normalized by the Alfvén time τ_A) of the resistive wall on the growth rates of the $n = 1$ and $n = 3$ ideal kink-peeling instabilities, assuming two equilibria with different edge safety factors. The plasma equilibrium flow is assumed zero.

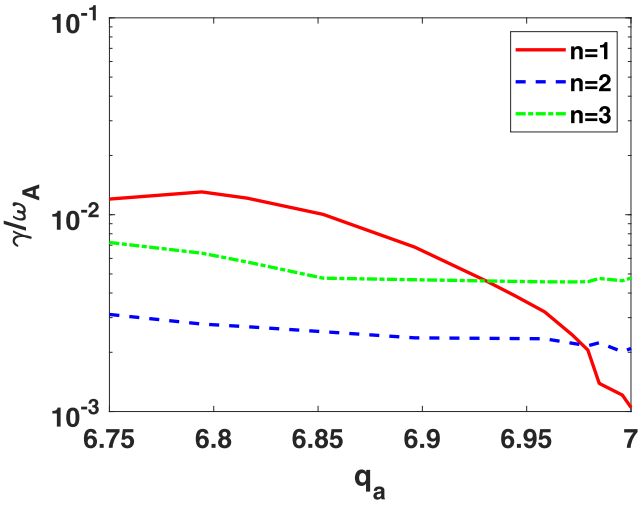

Figure 5. The MARS-F computed growth rate of the $n = 1, 2, 3$ resistive instabilities while slightly smoothing the plasma boundary shape near the X-point of the plasma separatrix, resulting in variation of the edge safety factor q_a with q_{95} being nearly unchanged. Assumed are the Spitzer resistivity for the plasma, the wall time of $\tau_w/\tau_A = 10^4$ for the resistive wall, and vanishing plasma equilibrium flow.

physics, associated with these three contributions, is the resonant matching between the corresponding particle drift frequencies—the toroidal precession frequency ω_d, the bounce frequency ω_b, and the transit frequency ω_t—and the mode (complex) frequency ω. The mode-particle resonance operator λ_{ml} in the particle phase space, for each poloidal harmonic m and bounce harmonic l, reads [18]

$$\lambda_{ml} = \frac{n[\omega_{*N} + (\hat{\epsilon_k} - 3/2)\omega_{*T} + \omega_E] - \omega}{n\omega_d + [\alpha(m + nq) + l]\omega_b - i\nu_{eff} - \omega}, \qquad (8)$$

where ω_{*N} and ω_{*T} are the diamagnetic drift frequencies due to the density and temperature gradients, respectively. ω_E is the $\mathbf{E} \times \mathbf{B}$ drift due to the equilibrium electrostatic potential. ω_d is the bounce-orbit-averaged toroidal precession drift frequency of particles, including the ∇B and curvature drifts and the ω_E drift. $\hat{\epsilon_k} = \epsilon_k/T$ is the particle kinetic energy normalized by the temperature. $\alpha = 1$ for passing particles, and $\alpha = 0$ for trapped particles. ν_{eff} is the effective collision frequency for particle species.

Due to the very small mass of electrons, the bounce and transit frequencies of thermal electrons are typically very high, resulting in negligible drift kinetic resonant contributions to p_g^B and p_g^C, respectively. Therefore, these two contributions will not be considered in the kinetic computations reported in this work.

The above closure for the perturbed pressure tensor is derived from the solution of the drift kinetic equations for the plasma thermal particle species (i.e. both thermal ions and electrons) in the continuous form (i.e. not via the particle-in-cell approach). The key steps of solving the drift kinetic equation, in a semi-analytic fashion in a generic toroidal geometry, have been outlined in reference [18]. The solution of the drift kinetic equation, i.e. the perturbed particle distribution functions assuming Maxwellian equilibrium distribution for thermal particles, is then directly used to evaluate the perturbed plasma pressure tensor, thus closing the lower moment MHD equations.

Note that we have introduced three coefficients, α_D, α_B and α_C, in equation (7). These are numerical factors facilitating (artificial) scan of the corresponding drift kinetic contributions. By scanning these parameters from 0 to 1, we gain a smooth transition from the fluid stability results to the full kinetic results. (Strictly speaking, the fluid compressibility coefficient Γ is scanned from 5/3 to 0, while scanning the above parameters from 0 to 1). This is numerically important but also physics-wise useful in interpreting the kinetic results. Furthermore, by setting the individual term(s) to zero, we can isolate the contribution from different drift kinetic resonances. This is the procedure followed in this study.

To study the non-linear interplay between MHD perturbations and the plasma flow, MARS-Q also solves the $n = 0$ toroidal momentum balance equation [22]

$$\frac{\partial L}{\partial t} = D(L) + T_{NTV} + T_{j\times b} + T_{rey} \qquad (9)$$

for the flux surface averaged toroidal momentum $L = \rho\langle R^2\rangle\Omega$. The surface average is defined as $\langle f\rangle \equiv \oint f\,dS/\oint dS$, where S is the flux surface. The first term in the right-hand side of equation (9), $D(L)$, represents a linear momentum diffusion operator [23]

$$D(L) = \frac{\partial}{\partial s}\chi_M\langle|\nabla s|^2\rangle\frac{\partial L}{\partial s} \qquad (10)$$

with χ_M being the toroidal momentum diffusion coefficient, which is a prescribed (input) quantity in the MARS-Q model. The expressions for latter three torques, i.e. the neoclassical toroidal viscous (NTV) torque, the resonant electromagnetic torque ($j \times b$) and the toroidal torque associated with the Reynolds stress tensor ('rey'), are the same as that described in

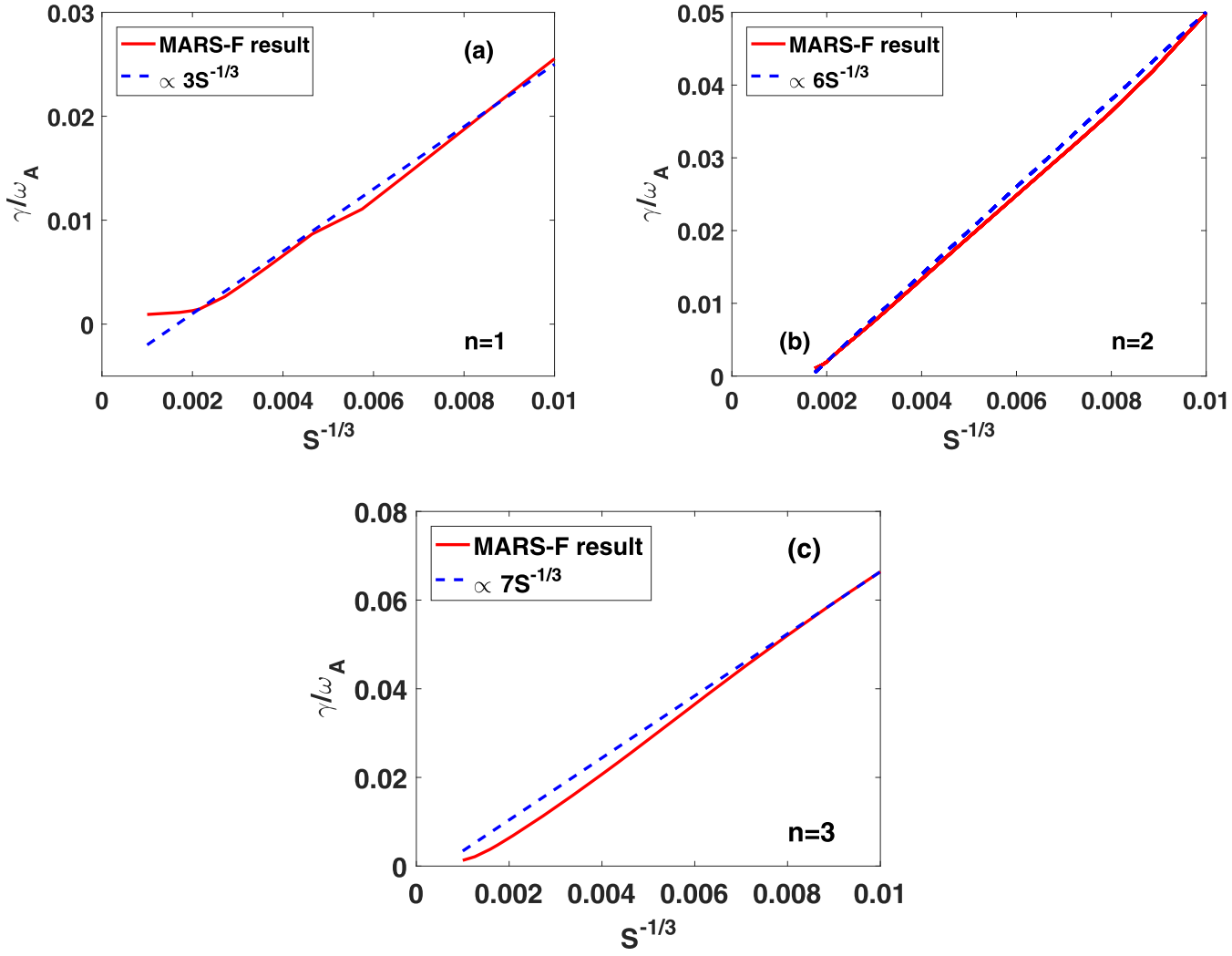

Figure 6. The MARS-F computed growth rates of the (*a*) $n = 1$, (*b*) $n = 2$, and (*c*) $n = 3$ resistive kink-peeling instabilities, while scanning the Lundquist number S. Considered is the equilibrium (with the edge safety factor $q_a = 6.985$) shown in figure 1. Assumed are the resistive wall with the wall time of $\tau_w/\tau_A = 10^4$ and vanishing plasma equilibrium flow.

reference [21]. In this work, all the linear stability results are obtained by running MARS-F/K as an eigenvalue solver, while the quasi-linear results presented in section 5 are obtained by running MARS-Q as an initial value solver.

Now we describe the plasma equilibrium assumed in this study (figure 1). This equilibrium is reconstructed from the DIII-D discharge 157102 at 2420 ms [12]. Figure 1(*a*) shows the plasma boundary shape, where the sharp tip associated with the X-point has been slightly smoothed, resulting in a finite value of $q_a = 6.985$ for the edge safety factor (figure 1(*b*)). Since the peeling mode stability is known to be sensitive to the edge safety factor [24, 25], we shall also systematically scan the plasma boundary shape near the X-point in this study. Figures 1(*c*) and (*d*) show the experimentally measured fluid rotation and $E \times B$ rotation profiles, respectively. Both rotation profiles, as well as their linear combinations, will be used as the MARS-Q input, to study the sensitivity of the kink-peeling mode instability against the flow model. In addition, the $E \times B$ rotation also enters into the MARS-K kinetic formulation, via the wave-particle resonance operator (8).

3. Linear stability analysis

We start by investigating the ideal kink-peeling instability without resistive wall and with vanishing plasma flow. Figure 2 shows the MARS-F computed growth rate for the $n = 1$–3 modes, while scanning the edge safety factor q_a. We emphasize that the q_a value here is varied by smoothing the plasma boundary shape near the X-point, as mentioned before. This procedure almost does not change the q_{95} value nor the q-values further inside the plasma. Evidently, the mode growth rate is sensitive to q_a, recovering the well known phenomenon of peeling mode stabilization by the separatrix geometry [26]. For further instability studies, we choose two equilibria with $q_a = 6.985$ and $q_a = 6.794$, respectively, with one being weakly unstable and the other being strongly unstable to the $(n = 1, 3)$ kink-peeling mode. Note that the $n = 2$ mode is always marginally unstable for this DIII-D equilibrium, independent of the q_a-value.

The modes are identified as the kink-peeling instability by examining the eigenmode structure for the radial

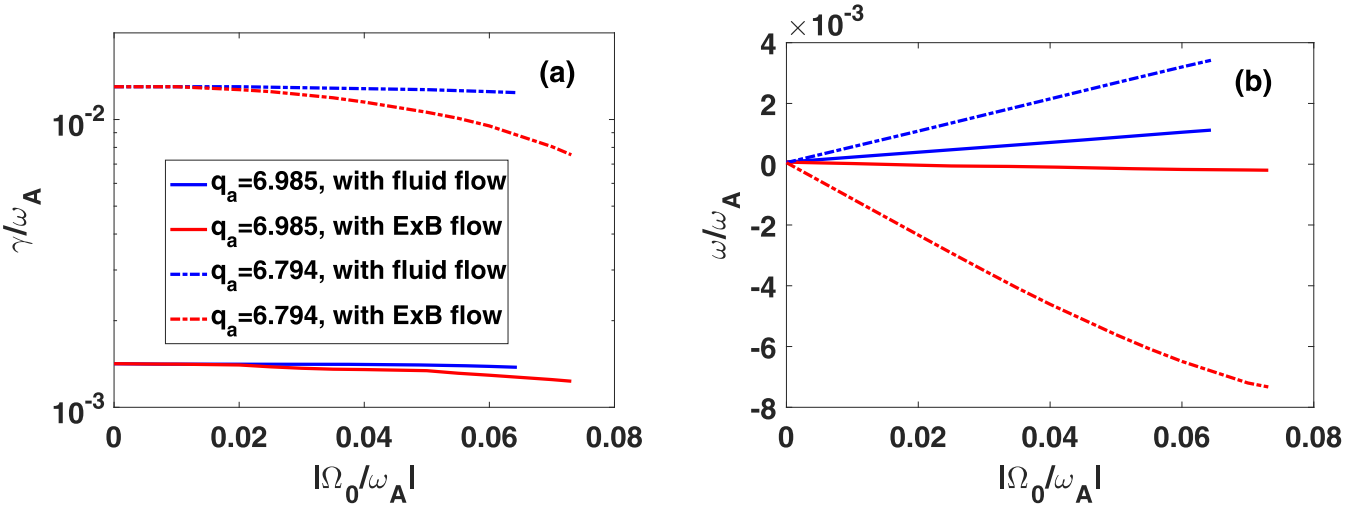

Figure 7. The computed (a) growth rate, and (b) mode frequency, for the $n = 1$ resistive kink-peeling mode, while varying the equilibrium toroidal rotation frequency. Considered are two equilibria with different edge safety factors and two toroidal flow models as shown in figures 1(c) and (d). Assumed are the resistive wall with the wall time of $\tau_w/\tau_A = 10^4$ and the Spitzer resistivity for the plasma (with the Lundquist number of $S = 1.867 \times 10^8$).

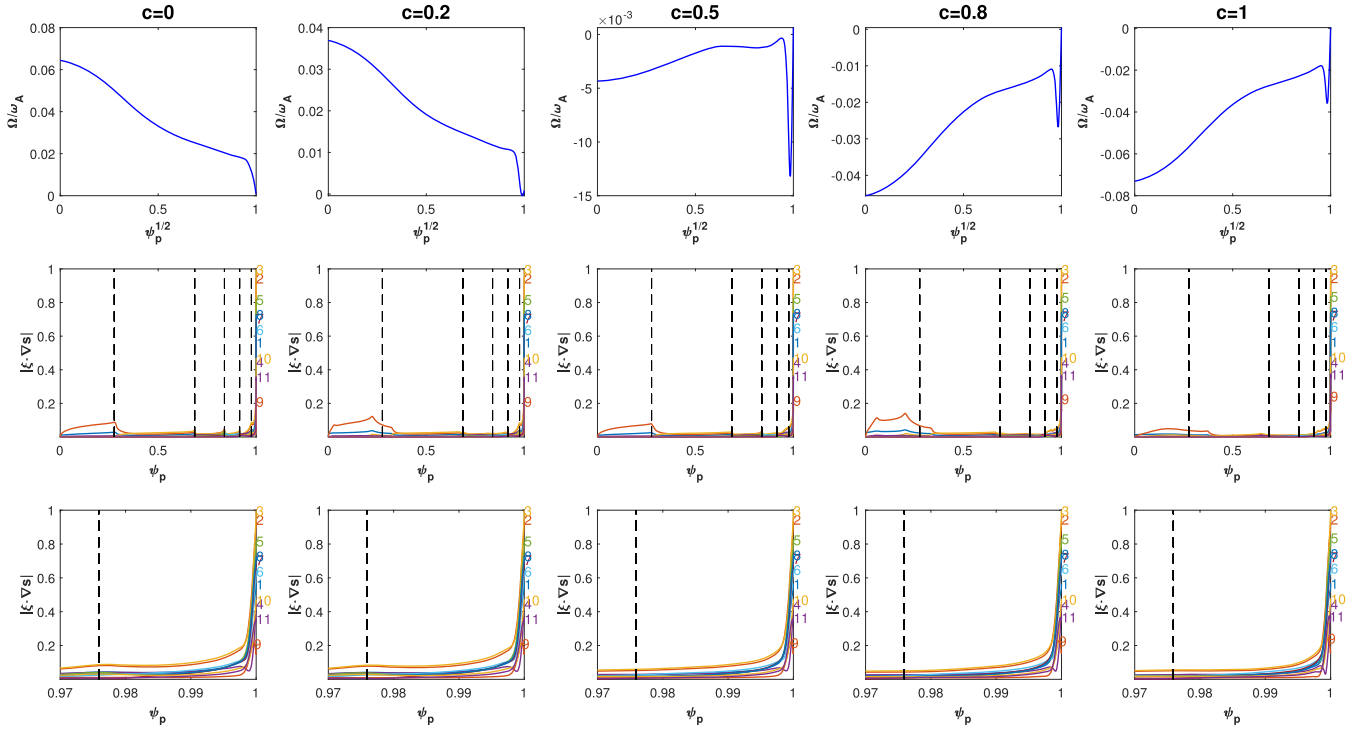

Figure 8. Effect of the plasma equilibrium flow model on the eigenmode structure of the $n = 1$ resistive kink-peeling instability. Shown are the toroidal rotation profiles (top panels), the poloidal Fourier harmonics of the radial displacement of the plasma (middle panels), and the zoomed-in radial displacement near the plasma edge (bottom panels). The linear interpolation factor c varies between 0 and 1, with $c = 0$ recovering the experimentally measured fluid flow (figure 1(c)) and $c = 1$ recovering the experimentally measured $E \times B$ flow (figure 1(d)). Assumed are the resistive wall with the wall time of $\tau_w/\tau_A = 10^4$, the equilibrium with the edge safety factor $q_a = 6.985$ and the Spitzer resistivity for the plasma (with the Lundquist number of $S = 1.867 \times 10^8$).

displacement of the plasma, as shown in figure 3. All instabilities are strongly localized near the plasma edge. In particular, the $n = 1$ and $n = 3$ instabilities exhibit typical peeling mode characteristics, which peaks at the plasma boundary for the radial displacement. The ideal $n = 2$ mode does not exactly peak at the plasma boundary, exhibiting a mode structure that is similar to that of the edge localized infernal mode [27]. This mode structure changes with inclusion of the plasma resistivity, as will be shown later on. It is also important to note the presence of multiple poloidal Fourier harmonics with large amplitude for all $n = 1$–3 perturbations, indicating a strong mode coupling effect.

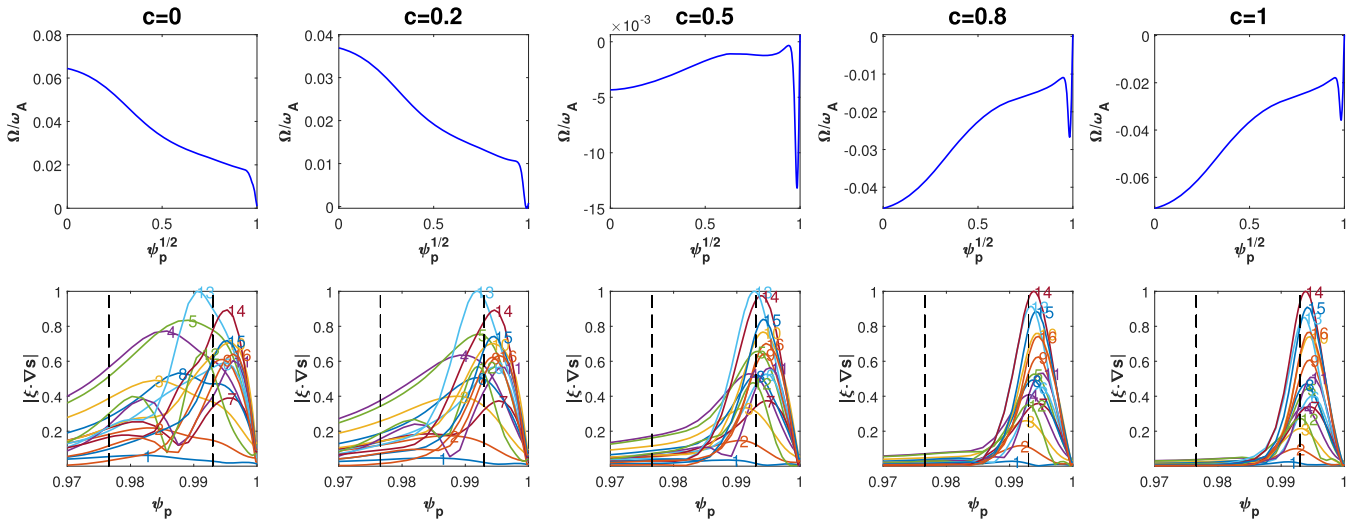

Figure 9. Effect of the plasma equilibrium flow model on the eigenmode structure of the $n = 2$ resistive kink-peeling instability. Shown are the toroidal rotation profiles (top panels) and the poloidal Fourier harmonics of the radial displacement (near the plasma edge) of the plasma (bottom panels). The linear interpolation factor c varies between 0 and 1, with $c = 0$ recovering the experimentally measured fluid flow (figure 1(c)) and $c = 1$ recovering the experimentally measured $E \times B$ flow (figure 1(d)). Assumed are the resistive wall with the wall time of $\tau_w/\tau_A = 10^4$, the equilibrium with the edge safety factor $q_a = 6.985$ and the Spitzer resistivity for the plasma (with the Lundquist number of $S = 1.867 \times 10^8$).

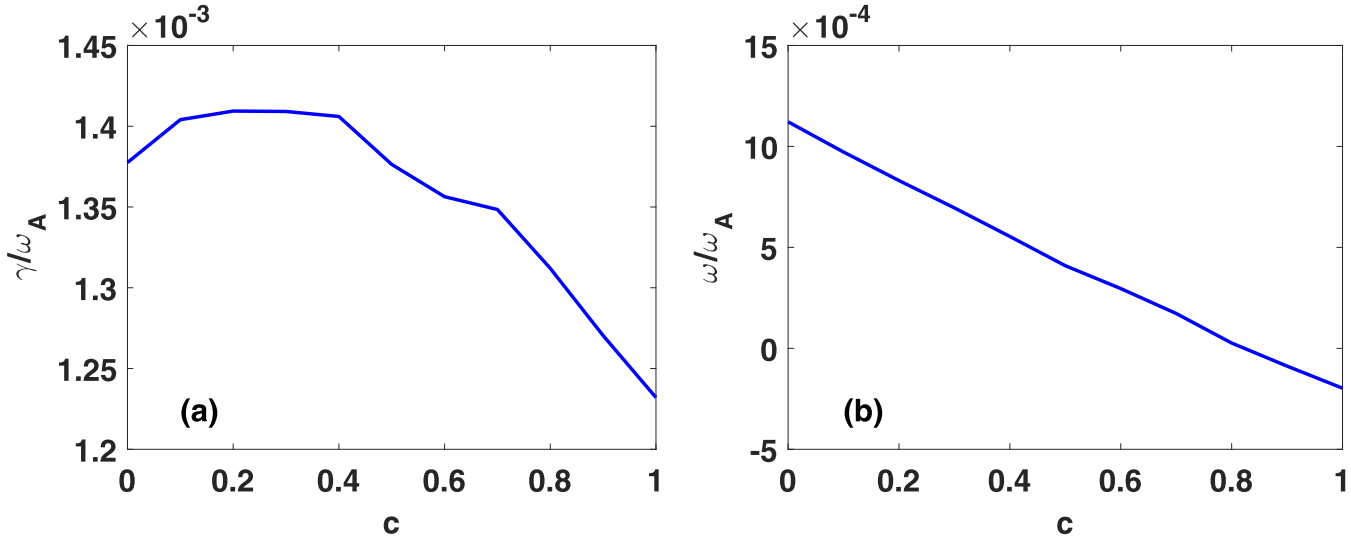

Figure 10. The computed (a) growth rate, and (b) mode frequency, of the $n = 1$ resistive kink-peeling instability, while varying the linear interpolation factor c from 0 and 1, with $c = 0$ recovering the experimentally measured fluid flow (figure 1(c)) and $c = 1$ recovering the experimentally measured $E \times B$ flow (figure 1(d)). Assumed are the resistive wall with the wall time of $\tau_w/\tau_A = 10^4$, the equilibrium with the edge safety factor $q_a = 6.985$ and the Spitzer resistivity for the plasma (with the Lundquist number of $S = 1.867 \times 10^8$).

We remark here that the extremely strong localization of the mode eigen-structure along the plasma minor radius poses numerical challenge for toroidal MHD codes. In MARS-F, this radial structure is resolved by employing very strong mesh packing near the plasma edge.

Next, we investigate various additional physics effects on the mode's linear instability, including the presence of a resistive wall, the plasma resistivity, the plasma toroidal flow, and finally the drift kinetic effects.

3.1. Effect of resistive wall

Here, we consider the two most unstable modes, i.e. $n = 1$ and $n = 3$. MARS-F computations reveal that the wall stabilization on these kink-peeling modes is weak. Figure 4 shows the computed mode growth rate while scanning the resistive wall time τ_w in a wide range. Note that the wall shape follows that of the DIII-D vacuum vessel (figure 1(a)). The wall time in the figure is normalized by the Alfvén time τ_A. The typical wall

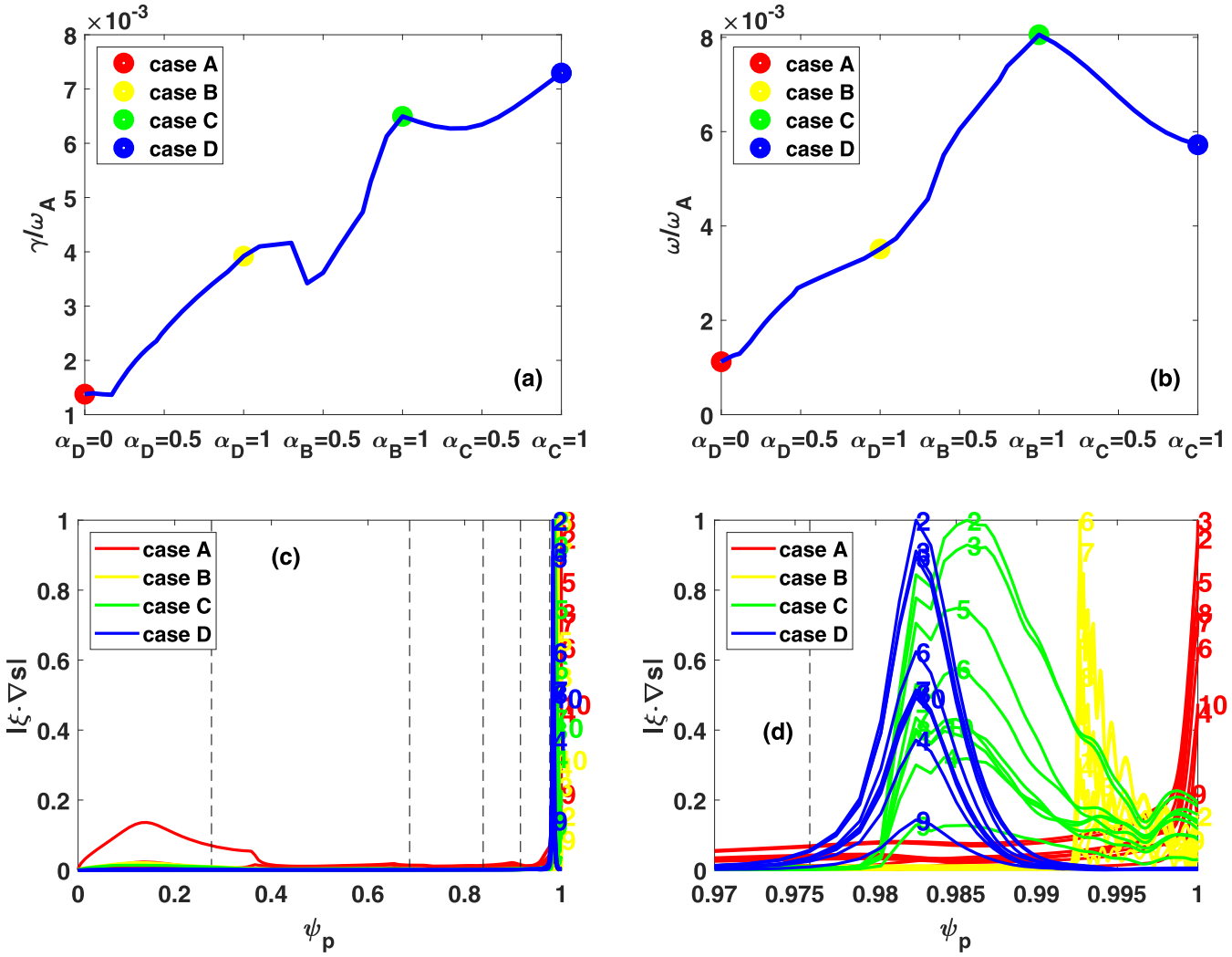

Figure 11. The MARS-K computed $n = 1$ kink-peeling instability with inclusion of various drift kinetic effects. Shown are (a) the mode growth rate, (b) the mode frequency, (c) poloidal harmonics of the radial displacement of the plasma, and (d) the zoomed-in radial displacement near the plasma edge. Case A (with $\alpha_D = \alpha_B = \alpha_C = 0$) corresponds to the fluid model. Case B (with $\alpha_D = 1, \alpha_B = \alpha_C = 0$) corresponds to the inclusion of the precessional drift effect of trapped thermal ions and electrons. Case C (with $\alpha_D = \alpha_B = 1, \alpha_C = 0$) corresponds to the inclusion of both precessional and bounce resonances of trapped particles. Case D (with $\alpha_D = \alpha_B = \alpha_C = 1$) corresponds to the inclusion of full drift kinetic effects from thermal particles. The vertical dashed lines indicate the radial location of the rational surfaces associated with the $n = 1$ perturbation. Assumed are the resistive wall with the wall time of $\tau_w/\tau_A = 10^4$, the equilibrium with the edge safety factor $q_a = 6.985$ and the Spitzer resistivity for the plasma (with the Lundquist number of $S = 1.867 \times 10^8$).

time for the DIII-D vacuum vessel, of several milliseconds, corresponds to $\tau_w/\tau_A \sim 10^4$.

The reason for the weak wall effect is that the magnetic perturbation, associated with these instabilities, decays fast outside the plasma boundary. Consequently, no significant eddy current is induced in the wall. This is again a typical behavior for the edge localized kink-peeling modes with high-m poloidal harmonics. Results shown in figure 4 thus indicate that the resistive wall effect can be largely neglected when studying these instabilities in DIII-D. Nevertheless, we keep $\tau_w/\tau_A = 10^4$ in the following studies, for the sake of accuracy.

3.2. *Effect of plasma resistivity*

The plasma resistivity, on the other hand, is found to strongly destabilize the kink-peeling modes, as reported in figure 5. With inclusion of the Spitzer resistivity, the higher-n mode becomes more unstable, as the edge safety factor approaches the integer number of $q_a = 7$. This is qualitatively different from the ideal MHD results shown in figure 2. Interestingly, the $n = 3$ mode growth rate now becomes less sensitive to q_a with inclusion of finite plasma resistivity. This is due to a fact that the peak of the $n = 3$ displacement shifts further away from the plasma edge (not shown here) due to finite plasma resistivity, i.e., becoming less peeling-like which should peak at the plasma boundary. Consequently, the role of the edge safety factor q_a is reduced and the plasma resistivity takes over in dictating the mode stability in this case.

Figure 6 shows the stability results for the $n = 1$–3 kink-peeling modes, where we scan the on-axis Lundquist number $S = \tau_R/\tau_A$ at fixed edge safety factor of $q_a = 6.985$. Here,

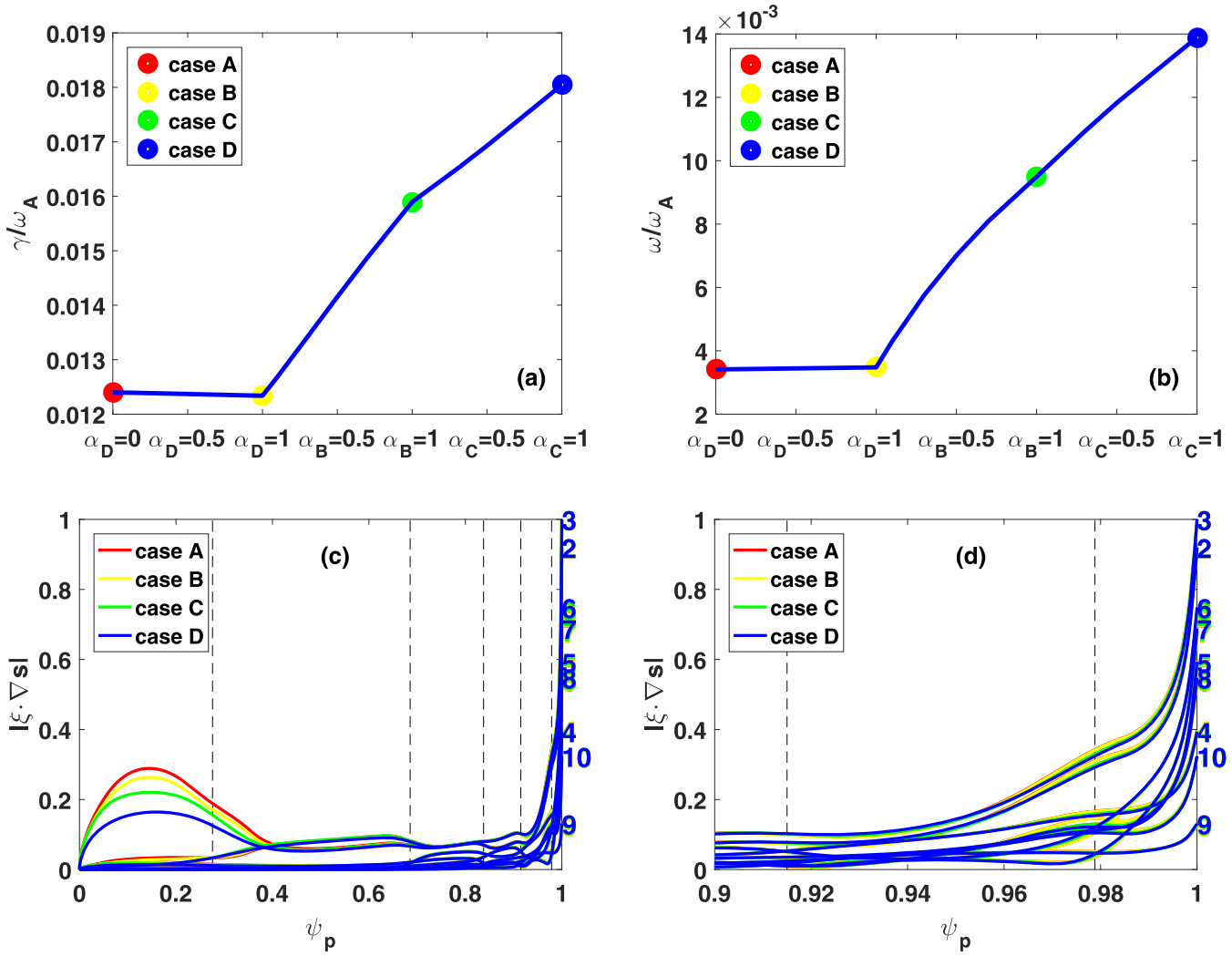

Figure 12. The MARS-K computed $n = 1$ kink-peeling instability with inclusion of various drift kinetic effects. Shown are (*a*) the mode growth rate, (*b*) the mode frequency, (*c*) poloidal harmonics of the radial displacement of the plasma, and (*d*) the zoomed-in radial displacement near the plasma edge. Case A (with $\alpha_D = \alpha_B = \alpha_C = 0$) corresponds to the fluid model. Case B (with $\alpha_D = 1, \alpha_B = \alpha_C = 0$) corresponds to the inclusion of the precessional drift effect of trapped thermal ions and electrons. Case C (with $\alpha_D = \alpha_B = 1, \alpha_C = 0$) corresponds to the inclusion of both precessional and bounce resonances of trapped particles. Case D (with $\alpha_D = \alpha_B = \alpha_C = 1$) corresponds to the inclusion of full drift kinetic effects from thermal particles. The vertical dashed lines indicate the radial location of the rational surfaces associated with the $n = 1$ perturbation. Assumed are the resistive wall with the wall time of $\tau_w/\tau_A = 10^4$, the equilibrium with the edge safety factor $q_a = 6.794$ and the Spitzer resistivity for the plasma (with the Lundquist number of $S = 1.867 \times 10^8$).

$\tau_R = \mu_0 a^2/\eta_0$ is the resistive decay time of the plasma current and a the plasma minor radius. The radial profile of the plasma resistivity η follows the Spitzer model

$$\eta = \eta_0 [T_e/T_e(0)]^{-3/2}, \tag{11}$$

where $\eta_0 \equiv \eta(0)$ is the on-axis resistivity value and T_e the thermal electron temperature. For the DIII-D plasma conditions considered here, the on-axis S-value for the Spitzer resistivity is calculated as 1.87×10^8.

The most interesting result from figure 6 is the roughly $S^{-1/3}$ scaling for the mode growth rate, for all $n = 1, 2, 3$ modes. This numerically obtained scaling is different from that for the typical tearing mode, which scales as $S^{-3/5}$ (in the absence of the favorable average curvature stabilization effect). We note that similar scaling of $S^{-1/3}$ also holds for other resistive MHD modes such as the resistive internal kink or the edge localized infernal mode [27]. We mention that the plasma resistivity strongly affects the mode growth rate but not the eigenmode structure. The latter remains similar to that shown in figure 3.

3.3. Effect of plasma flow

Next, we study the influence of the plasma toroidal equilibrium flow on the kink-peeling mode stability. The flow profiles are taken from experiments as shown in figure 1. Since the fluid and the $E \times B$ rotation frequencies substantially differ (even by sign) in this DIII-D plasma, we consider both rotations as well as their linear combinations. The goal here is to clarify, in a systematic manner, the effect on the mode stability, by assuming different flow models.

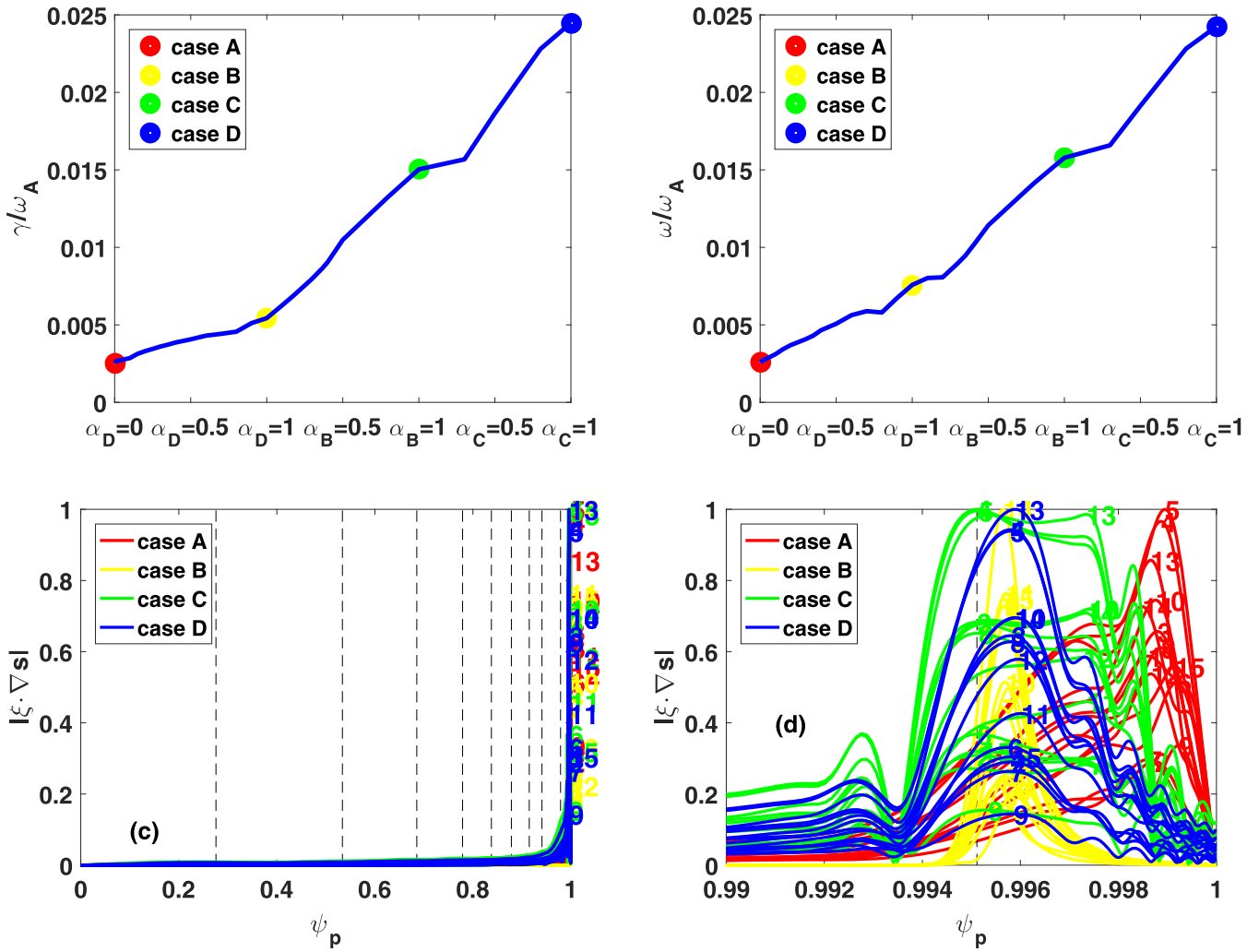

Figure 13. The MARS-K computed $n = 2$ kink-peeling instability with inclusion of various drift kinetic effects. Shown are (*a*) the mode growth rate, (*b*) the mode frequency, (*c*) poloidal harmonics of the radial displacement of the plasma, and (*d*) the zoomed-in radial displacement near the plasma edge. Case A (with $\alpha_D = \alpha_B = \alpha_C = 0$) corresponds to the fluid model. Case B (with $\alpha_D = 1, \alpha_B = \alpha_C = 0$) corresponds to the inclusion of the precessional drift effect of trapped thermal ions and electrons. Case C (with $\alpha_D = \alpha_B = 1, \alpha_C = 0$) corresponds to the inclusion of both precessional and bounce resonances of trapped particles. Case D (with $\alpha_D = \alpha_B = \alpha_C = 1$) corresponds to the inclusion of full drift kinetic effects from thermal particles. The vertical dashed lines indicate the radial location of the rational surfaces associated with the $n = 2$ perturbation. Assumed are the resistive wall with the wall time of $\tau_w/\tau_A = 10^4$, the equilibrium with the edge safety factor $q_a = 6.794$ and the Spitzer resistivity for the plasma (with the Lundquist number of $S = 1.867 \times 10^8$).

Figure 7 compares the computed mode growth rate and frequency for the $n = 1$ mode, while scanning the rotation amplitude up to the experimental values while fixing the radial profile. The experimental on-axis fluid rotation frequency is $\Omega_0 = 207.6$ krad s^{-1}, corresponding to the normalized (by the Alfvén frequency $\omega_A \equiv 1/\tau_A$) value of 6.44×10^{-2}. The experimental on-axis $E\times B$ rotation frequency is $\Omega_0 = -235.5$ krad s^{-1}, corresponding to the normalized value of -7.31×10^{-2}. Note that even though the on-axis rotation frequency is scanned here, what matters more is the pedestal rotation for the kink-peeling instability. By scanning the on-axis rotation while keeping the overall radial profile fixed, we are effectively changing the pedestal flow.

Figure 7 shows that both rotation models yield similar stabilization effect on the mode. The stabilization is not particularly strong though. The only significant difference is the mode frequency, which changes sign between the fluid and the $E \times B$ flow models. This is because, within the single fluid description, this type of localized mode tends to rotate together with the plasma. The sign of the mode frequency (in the laboratory frame) is thus dictated by the direction of the plasma rotation.

As a further step of investigation along this direction, we consider a series of new rotation profiles, via linear combination of the two extreme cases—the experimentally measured fluid and $E \times B$ rotations

$$\Omega_{\text{new}} = (1 - c) * \Omega_{\text{fluid}} + c * \Omega_{E\times B}, \tag{12}$$

where Ω_{fluid} and $\Omega_{E\times B}$ are shown in figures 1(*c*) and (*d*), respectively. Note that we use formula (12) to mix two flows not to separate them. More specifically, this formula recovers

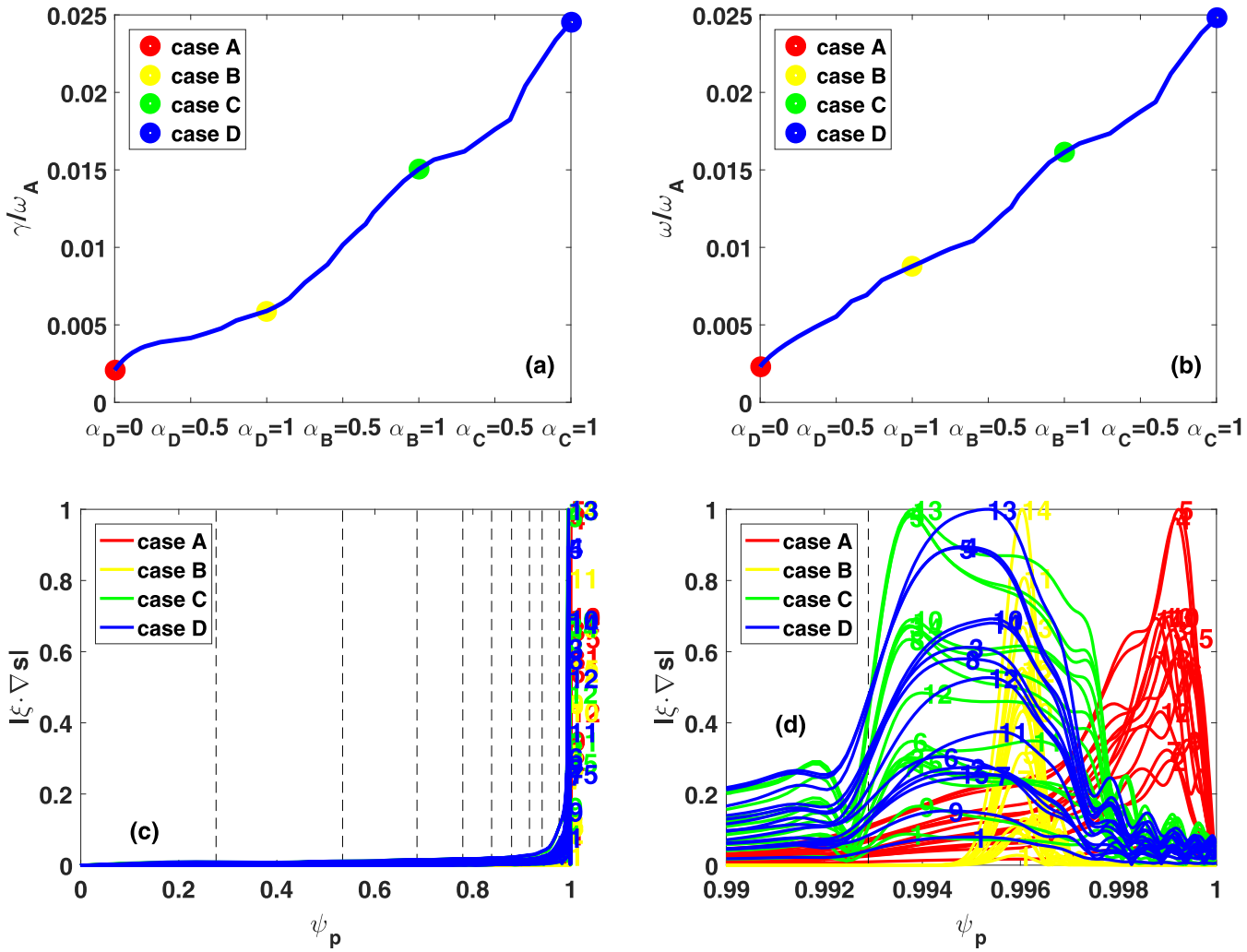

Figure 14. The MARS-K computed $n = 2$ kink-peeling instability with inclusion of various drift kinetic effects. Shown are (*a*) the mode growth rate, (*b*) the mode frequency, (*c*) poloidal harmonics of the radial displacement of the plasma, and (*d*) the zoomed-in radial displacement near the plasma edge. Case A (with $\alpha_D = \alpha_B = \alpha_C = 0$) corresponds to the fluid model. Case B (with $\alpha_D = 1, \alpha_B = \alpha_C = 0$) corresponds to the inclusion of the precessional drift effect of trapped thermal ions and electrons. Case C (with $\alpha_D = \alpha_B = 1, \alpha_C = 0$) corresponds to the inclusion of both precessional and bounce resonances of trapped particles. Case D (with $\alpha_D = \alpha_B = \alpha_C = 1$) corresponds to the inclusion of full drift kinetic effects from thermal particles. The vertical dashed lines indicate the radial location of the rational surfaces associated with the $n = 2$ perturbation. Assumed are the resistive wall with the wall time of $\tau_w/\tau_A = 10^4$, the equilibrium with the edge safety factor $q_a = 6.985$ and the Spitzer resistivity for the plasma (with the Lundquist number of $S = 1.867 \times 10^8$).

one of the flows at two limiting choices ($c = 0$ or $c = 1$) for the scaling parameter c. The sole idea here is to use this interpolation to smoothly trace the stability results from one flow model to the other. What happens in between is certainly of less physics significance.

Figure 8 illustrates the change in the eigenmode structure, for a selected values of c. As c increases toward 1 (the $E \times B$ flow model), the mode becomes more localized near the plasma edge, with decreasing core displacement. Even more obvious edge localization with increasing c is reported in figure 9 for the $n = 2$ mode. This shows that the plasma toroidal flow affects not only the mode stability but also the mode structure. These two aspects are of course coupled in consistent toroidal computations.

The mode eigenvalue for the $n = 1$ instability is plotted in figure 10, with varying interpolation parameter c for the flow profile. It is evident that the influence of the flow profile on the mode growth rate is weak. The effect is much more pronounced on the mode frequency, which roughly follows the local rotation frequency (both in the amplitude and the direction) of the plasma. Similar observations are made for the $n = 2$ and $n = 3$ kink-peeling modes.

3.4. Drift kinetic effect

In this subsection, we investigate the drift kinetic effects from thermal particles on the stability of the $n = 1$ and $n = 2$ kink-peeling modes in this DIII-D plasma. The effect of energetic particles is neglected. Given the fact that the mode is highly localized near the plasma edge, it is not plausible that energetic ions can have substantial influence on the mode. The MHD-kinetic hybrid code MARS-K is utilized for the study, running with a non-perturbative formulation as described in section 2.

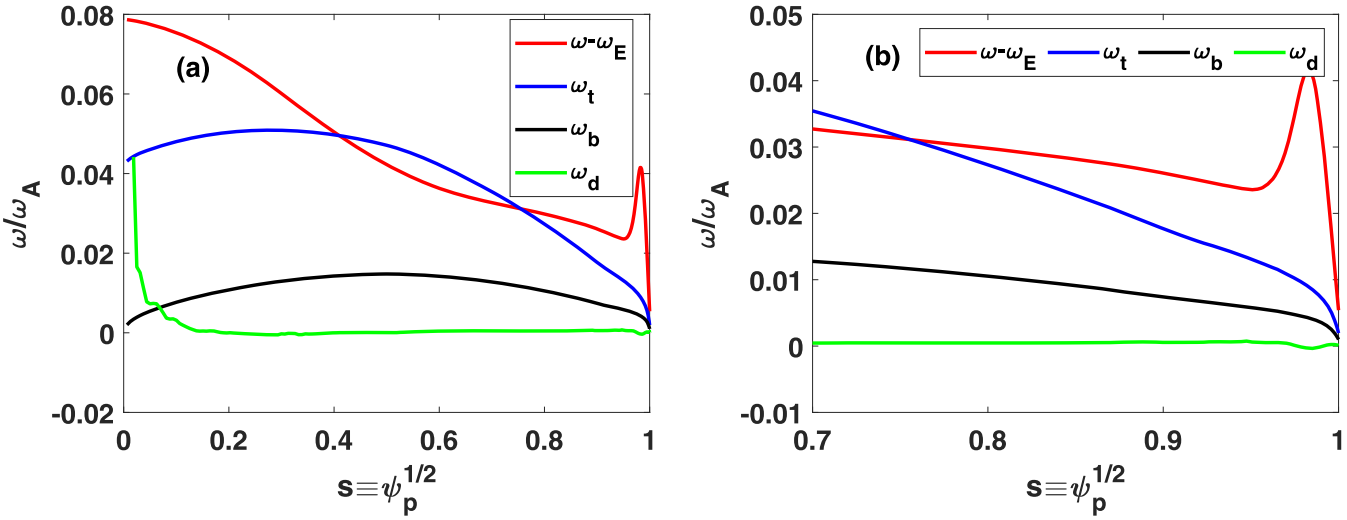

Figure 15. Comparison of various typical drift frequencies (a) along the plasma minor radius, and (b) near the plasma edge, including the $E \times B$-shifted mode frequency $\omega - \omega_E$, the transit frequency ω_t of passing thermal ions, the bounce frequency ω_b of trapped thermal ions, and the toroidal precessional frequency ω_d of trapped thermal ions due to the ∇B and curvature drifts. All the frequencies are normalized by the toroidal Alfvén frequency ω_A.

The key kinetic physics effects included here are (i) the precessional drift resonance of trapped thermal ions and electrons (associated with a drift kinetic parameter α_D as described in equation (7)), (ii) the bounce resonance of trapped thermal ions (α_B), and (iii) the transit resonance of circulating thermal ions (α_C).

Our procedure of investigation is as follows. We start with the fluid results reported in previous sections. We then progressively add the aforementioned three layers of drift kinetic effects, by scanning the associated fraction parameters α_D, α_B and α_C from 0 to 1 in a consecutive manner. The starting point of $\alpha_D = \alpha_B = \alpha_C = 0$ corresponds to the fluid result. The final point of $\alpha_D = \alpha_B = \alpha_C = 1$ corresponds to full inclusion of all the three types of drift kinetic resonances mentioned above.

Assuming $q_a = 6.985$, figures 11(a) and (b) reports the MARS-K computed growth rate and mode frequency, respectively, of the $n = 1$ peeling instability for this DIII-D equilibrium. Note that continuous scan of the fraction factors allows us to trace the physical branch of the mode in the complex plane for the eigenvalue. The physically more meaningful eigenvalues are of course those four points with α_D, α_B and α_C being either 0 or 1, denoted as points A–D. For this DIII-D plasma, MARS-K finds generally destabilizing effect of the drift kinetic resonances on the mode.

Within the non-perturbative MHD-kinetic hybrid approach, the eigenfunction of the mode is modified by the drift kinetic effects. This is demonstrated in figures 11(c) and (d), for all four physical cases A–D. Compared to the fluid eigenfunction (case A), the kinetic effects push the mode further away from the plasma boundary and toward the pedestal region, as shown in figure 11(d). We note that, despite the kinetic effect induced inward shift of the radial location of the peak of the eigenfunction, the mode is still located extremely close to the plasma boundary (figure 11(c)).

The eigenmode structure is substantially different for more unstable peeling mode, obtained with stronger smoothing of the plasma boundary near the X-point, resulting in $q_a = 6.794$ instead of 6.985 as for cases shown in figure 11. The plasma displacement is still largely peaked near the edge (figure 12(c)), but now covers a much wider radial range (figure 12(d)) compared to that shown in figure 11(d). More importantly, drift kinetic modification of the mode eigenfunction is very weak. Consequently, the eigenfunction computed within the fluid theory serves as a robust representation for the structure of the mode in these cases.

Figures 13 and 14 report the drift kinetic results for the $n = 2$ mode, assuming two different q_a values. In both cases, kinetic effects push the peaking of the mode eigenfunction inward, similar to that shown for the $n = 1$ mode at $q_a = 6.985$. On the other hand, a much stronger kinetic effects induced destabilization occurs for the $n = 2$ mode, compared to that of the $n = 1$ mode. The computed frequency of the $n = 2$ mode is about 12.8 kHz with inclusion of the full drift kinetic effects (case D), and this frequency value is almost independent of q_a. This is also different from the $n = 1$ mode, where 3 kHz and 7 kHz mode frequencies are driven by the kinetic effects, at $q_a = 6.985$ and $q_a = 6.794$, respectively. At $q_a = 6.794$, the $n = 2$ mode frequency roughly doubles that of the $n = 1$ mode, resembling more the EHO features as observed in experiments.

Drift kinetic modification of the kink-peeling mode stability, as reported above, can be partially understood by examining the mode-particle resonance conditions. Figure 15 compares various drift frequencies for the equilibrium at $q_a = 6.985$. Note that the precession (ω_d), bounce (ω_b) and transit (ω_t) frequencies are all obtained by averaging over the particle velocity space with the equilibrium (Maxwellian) distribution function as the weighting function. The precessional drift frequency, ω_d here, is due to the ∇B and curvature drifts. The mode frequency ω is computed for the $n = 1$ kink-peeling

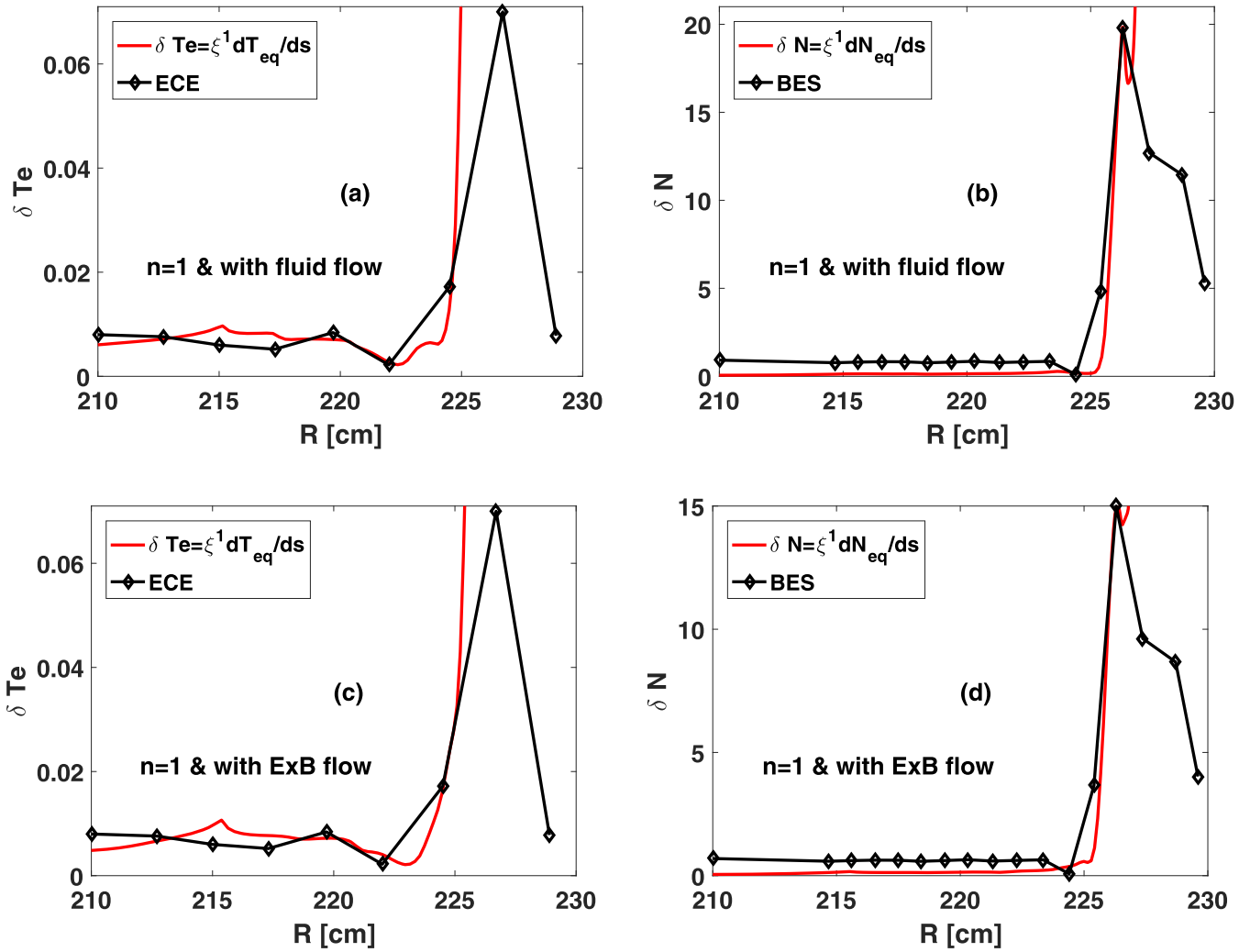

Figure 16. Comparison between the MARS-F computed internal perturbation data (solid red lines) and the experimental measurements (black lines with dots), for the $n = 1$ resistive kink-peeling mode. Considered are both (*a*) and (*c*) the electron temperature fluctuation measured by the electron cyclotron emission (ECE), and (*b*) and (*d*) the plasma density fluctuation measured by the beam emission spectrum (BES). Assumed for the toroidal flow model is either (*a*) and (*b*) the fluid rotation or (*c*) and (*d*) the $E \times B$ rotation. Assumed are the resistive wall with the wall time of $\tau_w/\tau_A = 10^4$, the equilibrium with the edge safety factor $q_a = 6.985$ and the Spitzer resistivity for the plasma (with the Lundquist number of $S = 1.867 \times 10^8$).

instability with inclusion of the full drift kinetic contributions (case D from figure 11). Generally, the Doppler shifted perturbation frequency, $\omega - \omega_E$, is different from the various drift frequencies shown in figure 15(*a*) in the bulk plasma region, excluding the possibility of significant drift kinetic resonances. On the other hand, these frequencies better match near the very edge of the plasma (figure 15(*b*)), yielding kinetic resonances between the mode and thermal particle drifts. Since the kink-peeling mode is strongly localized near the plasma edge, all three types of kinetic resonance contributions affect the mode stability, as shown in figure 11.

4. Comparison with experimental data

In what follows, we compare the MARS-F/K computed 'synthetic' diagnostic data with the experimental measurements, based on the eigenfunctions of the linear instability. Because the amplitude of the eigenfunction is not determined, we mainly compare the spatial structure of the perturbations, while matching the overall amplitude by re-normalizing the eigenfunction. We will compare both the internal (perturbed density and temperature) and external (magnetic perturbations) measurements. Both the fluid and kinetic kink-peeling results will be compared with experiments. Based on the MARS-F/K computed plasma radial displacement ξ^1, we construct the temperature and density fluctuations, δT_e and δN, respectively, via the commonly used relations in experiments

$$\delta T_e = \xi \cdot \nabla T_{e,eq} = (\xi \cdot \nabla s)\frac{dT_{e,eq}}{ds} = \xi^1 \frac{dT_{e,eq}}{ds} \quad (13)$$

$$\delta N = \xi \cdot \nabla N_{eq} = \xi^1 \frac{dN_{eq}}{ds}, \quad (14)$$

where $T_{e,eq}$ is the equilibrium thermal electron temperature and N_{eq} the equilibrium electron density, and s represents the radial coordinate (labeling equilibrium magnetic flux surfaces).

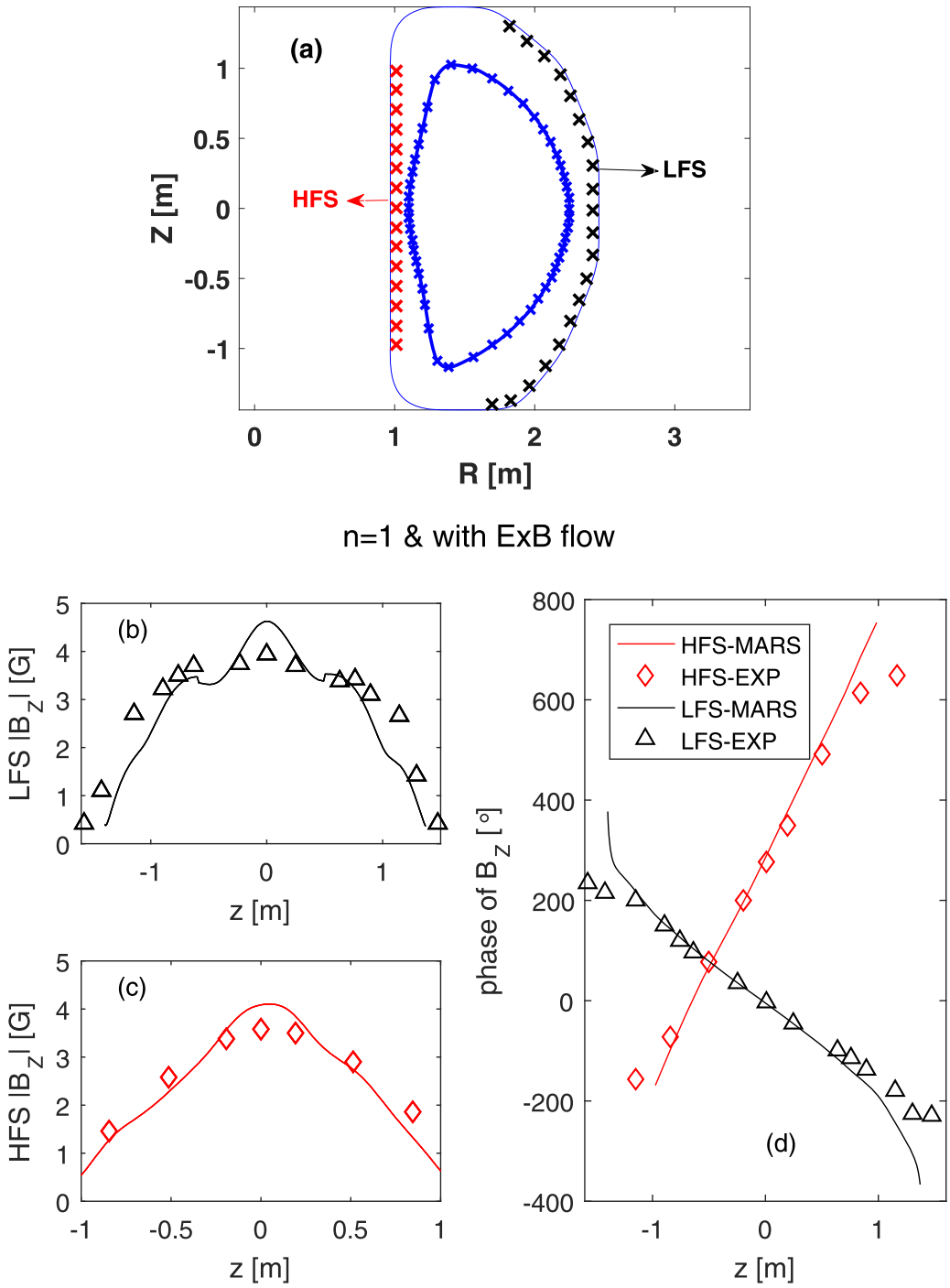

Figure 17. Comparison of the $n = 1$ poloidal magnetic field perturbation as measured at the locations indicated by 'x' in plot (a), along the vertical axis Z for the perturbation amplitude at (b) the LFS, and (c) the HFS, between the MARS-F modeling (solid lines) and experiments (open symbols). Compared in (d) is the toroidal phase of the $n = 1$ perturbation. The perturbation in the modeling is produced by the $n = 1$ resistive kink-peeling mode, assuming the resistive wall with the wall time of $\tau_w/\tau_A = 10^4$, the equilibrium with the edge safety factor $q_a = 6.985$ and the $E \times B$ toroidal flow, and the Spitzer resistivity for the plasma (with the Lundquist number of $S = 1.867 \times 10^8$).

Figure 16 compares δT_e and δN along the outboard midplane major radius (as adopted for the measured data), between the simulation and the experiment, associated with the $n = 1$ kink-peeling instability. Compared are the MARS-F results where we have assumed the Spitzer plasma resistivity model as well as a resistive wall with typical wall time as in DIII-D. Note that we have also assumed either the fluid rotation (figure 1(c)) or the $E \times B$ rotation (figure 1(d)) as measured in the experiment, as input to MARS-F. With either rotation profile, a reasonably good agreement is obtained between modeling and experiment, despite the large difference between these two rotation profiles. This shows that the density and temperature fluctuations are not sensitive to the plasma flow in this case. We also note that these fluctuations are localized very close to the plasma edge, as shown by both the measurement data and by the MARS-F modeling.

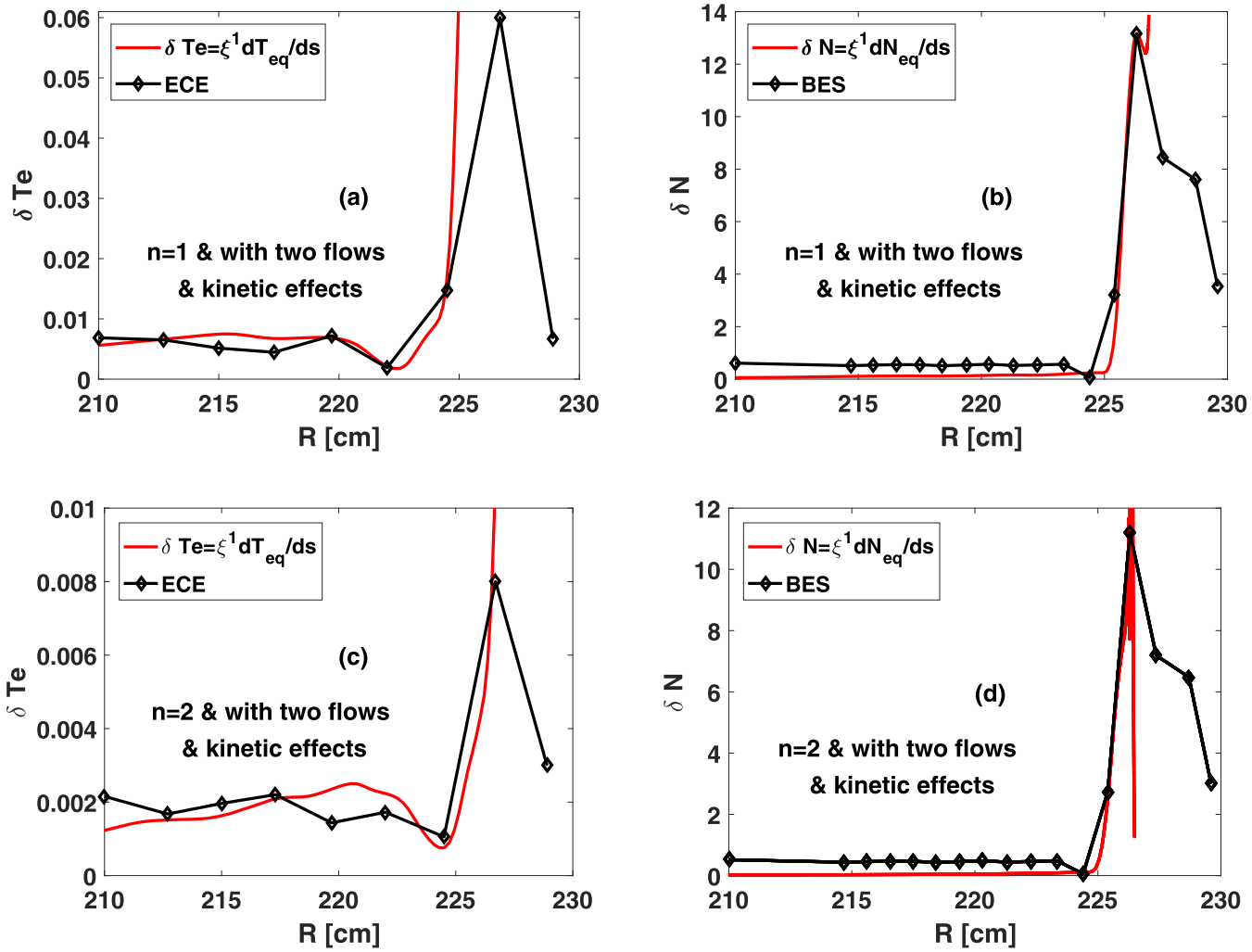

Figure 18. Comparison between the MARS-K computed internal perturbation data (solid red lines) and the experimental measurements (black lines with dots), for (*a*) and (*b*) the $n = 1$, and (*c*) and (*d*) the $n = 2$, kink-peeling mode. Considered are both (*a*) and (*c*) the electron temperature fluctuation measured by the ECE, and (*b*) and (*d*) the plasma density fluctuation measured by the BES. Full drift kinetic effects from thermal particles are included into the modeling, assuming the resistive wall with the wall time of $\tau_w/\tau_A = 10^4$, the equilibrium with the edge safety factor $q_a = 6.794$ and the Spitzer resistivity for the plasma (with the Lundquist number of $S = 1.867 \times 10^8$).

We make two additional remarks here. (i) For this DIII-D discharge, the plasma separatrix is located near $R = 226$ cm. The measured data outside $R = 226$ cm cannot be recovered by MARS-F/K, since the codes treat the region outside the plasma separatrix as pure vacuum. (ii) Although reported in figure 16 are the modeling results with $q_a = 6.985$, we mention that similar comparison has also been made assuming $q_a = 6.794$. A similarly good agreement is obtained, indicating the robustness of the modeled perturbation structure against variation of the plasma boundary shape near the X-point that we assume. The mode growth rate, on the other hand, is more sensitive to q_a as reported before.

Next, we compare the magnetic data between modeling and experiment. There are a set of magnetic probes installed just inside the DIII-D vacuum vessel wall, measuring the perturbed poloidal field component [28]. The geometrical location of these magnetic probes, both from the high field side (HFS) (red 'X') and the low field side (LFS) (black 'X') are indicated in figure 17(*a*). Figures 17(*b*)–(*d*) compares the $n = 1$ poloidal field perturbation amplitude and toroidal phase along the vertical location of the magnetic probes, between modeling and experiment. The point-wise value of the perturbed field is plotted for the modeling results. A good agreement is again obtained. We emphasize again that the overall perturbation amplitude from the modeling side is scaled to match the experiment. Therefore, the agreement shown in figures 17(*b*) and (*c*) is manifested only in the spatial structure. The toroidal phase of the perturbation field (figure 17(*d*)), however, is independent of the re-normalization of the perturbation amplitude. The $E \times B$ rotation profile has been assumed in this comparison, though similar degree of agreement is also obtained with the fluid flow, indicating that the magnetic fluctuation is not sensitive to the plasma flow either.

Although not shown here, we report that agreement in the magnetic data has also been found for the $n = 2$ perturbations, between the MARS-F modeling results and the experiment. In fact, comparison of the spatial mode structures, for both $n = 1$

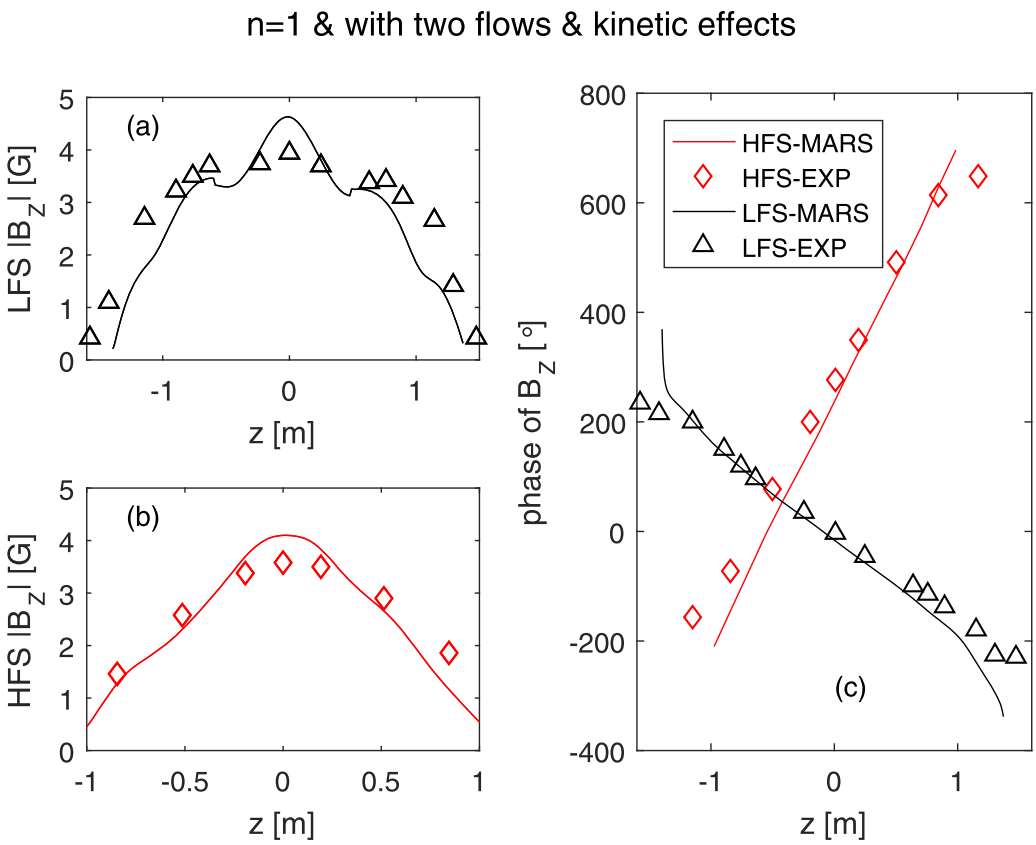

Figure 19. Comparison of the $n = 1$ poloidal magnetic field perturbation as measured at the locations indicated by 'x' in figure 17(*a*), along the vertical axis Z for the perturbation amplitude at (*a*) the LFS, and (*b*) the HFS, between the MARS-K modeling (solid lines) and experiments (open symbols). Compared in (*c*) is the toroidal phase of the $n = 1$ perturbation. The perturbation in the modeling is produced by the $n = 1$ kink-peeling mode, computed by assuming the full drift kinetic effects from thermal particles, the resistive wall with the wall time of $\tau_w/\tau_A = 10^4$, the equilibrium with the edge safety factor $q_a = 6.794$, and the Spitzer resistivity for the plasma (with the Lundquist number of $S = 1.867 \times 10^8$).

and $n = 2$, will be shown below in the context of kinetic kink-peeling computations. In what follows, no systematic modeling is carried out for the $n = 3$ kink-peeling instability, due to lack of experimental measurements for the $n = 3$ perturbation structure to compare with.

Figure 18 compares the perturbed temperature and density between the MARS-K results and the experiment. Compared with the fluid model (figure 16), the MHD-kinetic hybrid model offers a slightly better agreement with the experiment, in terms of these internal perturbation structures. Note that the agreement is generally good for both the $n = 1$ and $n = 2$ perturbations. Note also that in the hybrid model, both experimental flows are used as the input: the fluid flow enters into the MHD portion of the model, while the $E \times B$ rotation enters into the drift kinetic resonance operators.

With the MARS-K computed kink-peeling mode eigenfunctions, the magnetic data are also re-constructed and compared with the experiments, as shown in figures 19 and 20, for the $n = 1$ and $n = 2$ modes, respectively. It is evident that the kinetic effects do not generally improve the agreement with the experiment, in terms of the magnetic field perturbations outside the plasma, as compared to the fluid model (figure 17). The overall agreement, in terms of both the spatial structure and the toroidal phase of the magnetic perturbations, remains however reasonably good independent of the computational models adopted for the kink-peeling instability.

5. Non-linear interaction between plasma flow and kink-peeling instability

We have so far been reporting the linear stability of the kink-peeling mode as computed by MARS-F and MARS-K, assuming a fixed plasma toroidal rotation as measured in experiments. On the other hand, as a key physics ingredient of EHOs, the kink-peeling instability non-linearly interacts with the plasma flow. This is exploited by the quasi-linear initial value simulations utilizing MARS-Q, with results reported below.

The 'free' parameters of our quasi-linear model are the momentum diffusion coefficient, χ_M from equation (10), and the initial perturbation amplitude A_0 for the kink-peeling instability. In this work, we choose χ_M at the ~ 0.1 m^2 s^{-1} level, corresponding to the typical value as measured in DIII-D experiments [29]. We carry out a set of MARS-Q simulations assuming different values for the initial perturbation amplitude A_0. The Spitzer model is again used for the plasma resistivity. The drift kinetic effects are neglected in these MARS-Q runs.

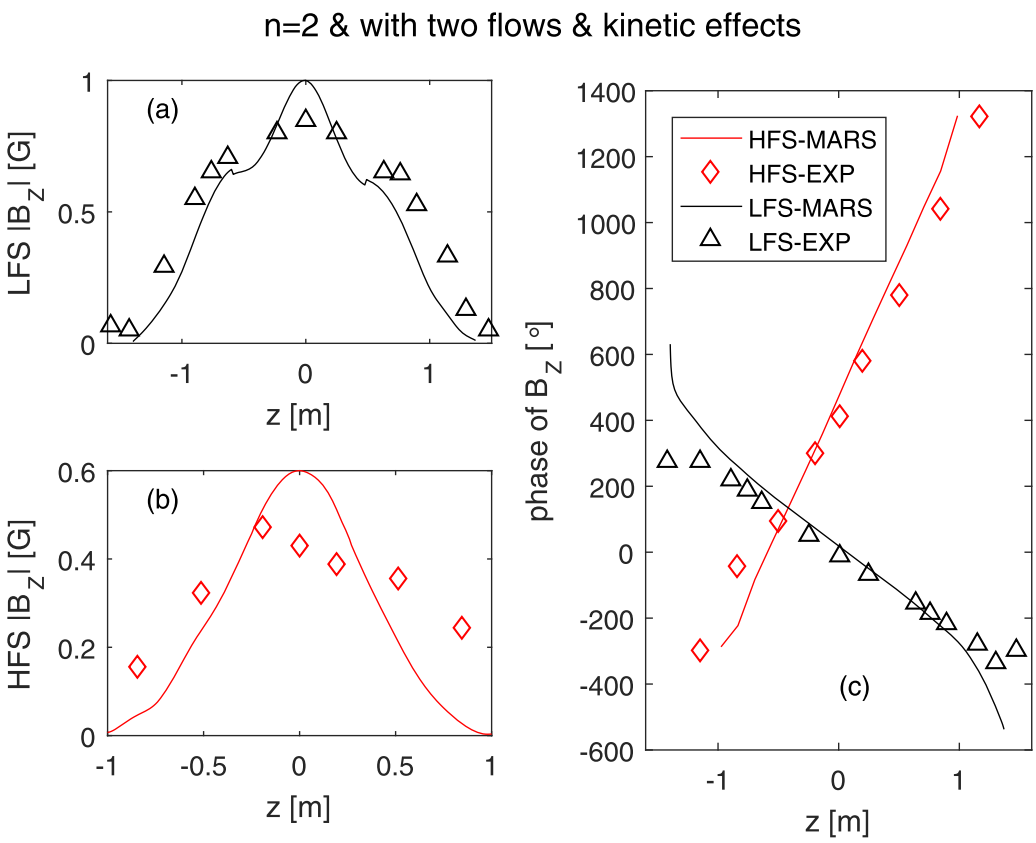

Figure 20. Comparison of the $n = 2$ poloidal magnetic field perturbation as measured at the locations indicated by 'x' in figure 17(a), along the vertical axis Z for the perturbation amplitude at (a) the LFS, and (b) the HFS, between the MARS-K modeling (solid lines) and experiments (open symbols). Compared in (c) is the toroidal phase of the $n = 2$ perturbation. The perturbation in the modeling is produced by the $n = 2$ kink-peeling mode, computed by assuming the full drift kinetic effects from thermal particles, the resistive wall with the wall time of $\tau_w/\tau_A = 10^4$, the equilibrium with the edge safety factor $q_a = 6.794$, and the Spitzer resistivity for the plasma (with the Lundquist number of $S = 1.867 \times 10^8$).

Figures 21(a) and (b) compares four sets of simulations for the $n = 1$ mode and with $q_a = 6.985$, assuming four different values for the initial perturbation amplitude A_0. Note that the A_0 value, defined in terms of the MARS-Q dimensionless quantity, provides a scaling factor for the overall initial perturbation. Therefore, the absolute value of A_0 is not of much physics significance. For a linearly unstable kink-peeling mode, we choose the linear mode eigenfunction for the initial perturbation. The simulation starts with the experimental rotation profile as shown in figure 1(c).

As a representative example for the evolution of the perturbed quantities, figure 21(a) shows time traces of the perturbed $m/n = 6/1$ resonant radial field component at the $q = 6$ rational surface. Since we started the simulations with the linear eigenfunction, the linear growth of the perturbation is well followed during the initial phase of the simulations (the growth rate re-constructed from such time traces recovers that from the eigenvalue computations). The most interesting part of the simulation, however, is the later phase when non-linear interplay between the perturbation and the plasma flow damping becomes substantial. As a result of this non-linear interaction, the $n = 1$ perturbation amplitude saturates, meanwhile the $n = 0$ flow amplitude (significantly) changes near the plasma edge (figure 21(b)). In other words, the $n = 1$ perturbation damps the $n = 0$ plasma flow (and modifies the flow shear) in this case, which in turn stabilizes the $n = 1$ kink-peeling instability. This saturation mechanism, which has previously been hypothesized to explain EHOs [10], is indeed confirmed here via toroidal numerical simulations.

It is important to note that the final saturated state is not sensitive to the initial perturbation amplitude that we assume. In fact, the initial amplitude mainly affects the simulation time it takes to reach the non-linear interaction stage and the quasi-steady state. This time scale is found to be relatively short—about ms according to the MARS-Q simulations. The toroidal rotation frequency decreases down to about -10 krad s^{-1} level in all four cases, before bouncing back to near the zero level. After reaching nearly vanishing (and saturated) rotation at the $q = 6$ surface, the simulation numerically crashes, probably due to lack of full non-linear MHD physics that are needed in order to resolve the time evolution. Full non-linear interaction among different toroidal harmonics, as well as the interaction between the MHD perturbations and the plasma toroidal flow, is beyond what the MARS-Q quasi-linear model can describe at present.

What we find also interesting is that the kink-peeling mode changes both the flow amplitude and flow shear near the plasma edge. One example of the flow profile evolution is

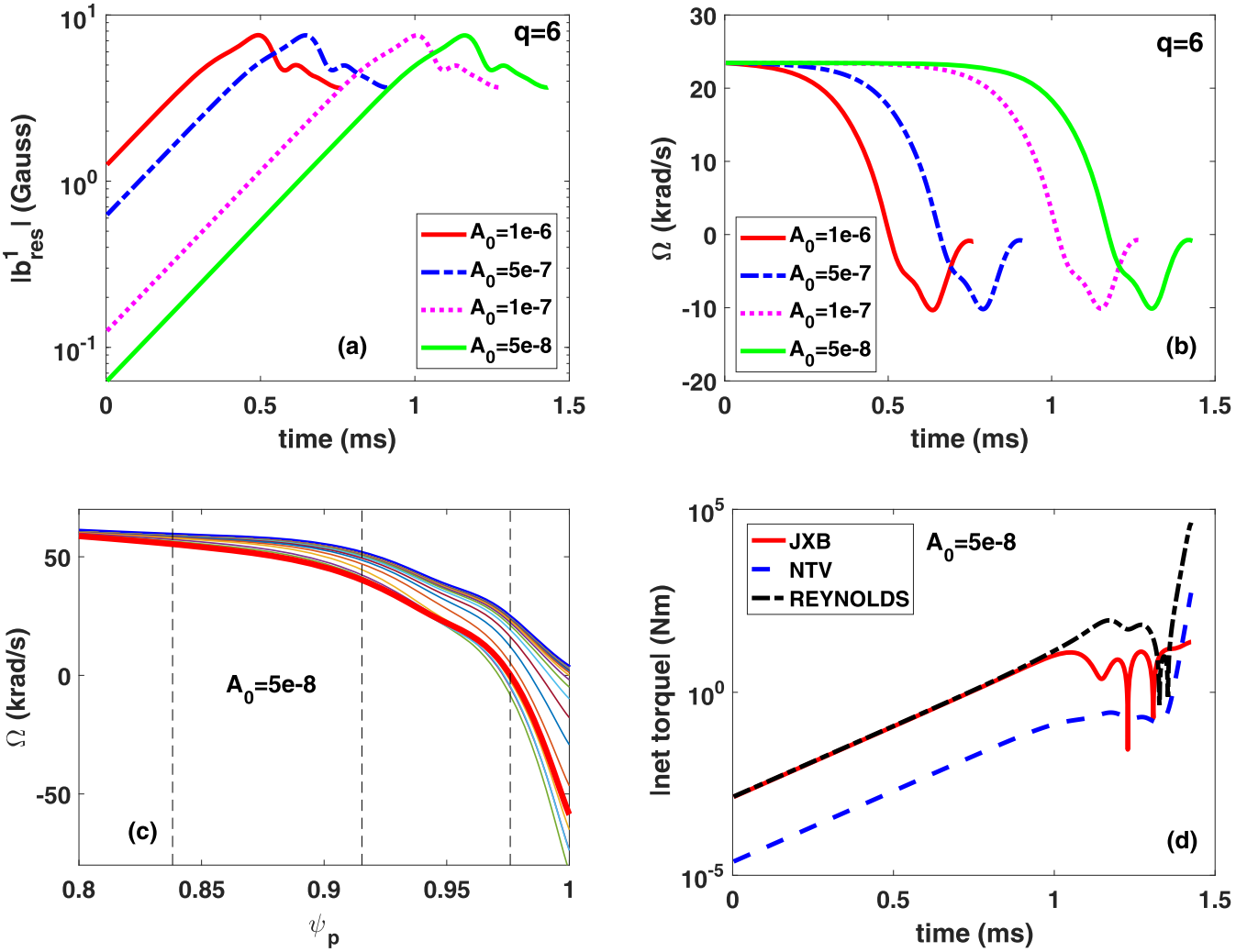

Figure 21. The MARS-Q simulated time traces of the initially unstable $n = 1$ resistive kink-peeling mode: (a) and (b) the perturbed $m/n = 6/1$ resonant radial field component and the toroidal rotation frequency, respectively, at the $q = 6$ rational surface, with different choices for the amplitude A_0 of the initial perturbation; (c) and (d) evolution of the rotation profile and the time traces of three toroidal net torques, respectively, assuming the initial perturbation amplitude of $A_0 = 5 \times 10^{-8}$. The thick blue (red) curve in (c) indicates the initial (final) rotation profile. The vertical dashed lines in (c) indicate locations of the rational surfaces associated with the $n = 1$ perturbation. The initial rotation profile is assumed to be the fluid rotation as shown in figure 1(c). Assumed are the toroidal momentum diffusion coefficient of $\chi_M = 0.1$ m^2 s^{-1}, the resistive wall with the wall time of $\tau_w/\tau_A = 10^4$, the equilibrium with the edge safety factor $q_a = 6.985$, and the Spitzer resistivity for the plasma (with the Lundquist number of $S = 1.867 \times 10^8$).

shown in figure 21(c), for the case with the initial amplitude of $A_0 = 5 \times 10^{-8}$. It is evident that the saturation of the kink-peeling mode (i.e. EHOs) is not simply caused by the reduction of the flow shear (which destabilizes the kink-peeling mode), as suggested by theory [10]. We note that flow shear destabilization of the low-n kink-peeling mode, being a well known effect, is not systematically investigated here. Flow shear often destabilizes macroscopic MHD instabilities such as the resistive wall mode, the internal kink, and the kink-peeling mode. The MARS-Q simulation here shows that the flow shear is effectively reduced due to the reduction of the flow amplitude near the $q = 6$ surface. This indicates that it is the combination of both the flow amplitude damping (across the zero-rotation point), and the change of the flow shear near the plasma edge, that leads to the stabilization and saturation of the kink-peeling mode in this DIII-D plasma, according to the MARS-Q modeling. The key role played here for the mode saturation is the local reduction of the flow shear. This physics mechanism is also different from that identified in reference [14] for EHOs, where not much change to the flow profile was reported.

The edge flow damping is caused by various toroidal torques associated with the kink-peeling instability. Figure 21(d) shows the time traces of the volume integrated toroidal torques associated with the Maxwell stress, the Reynolds stress and NTV. The Reynolds and the Maxwell stresses appear to play a large role in the initial flow damping. The NTV torque only becomes large toward the end of the simulation, when the toroidal rotation frequency approaches zero.

Qualitatively similar observations are made when we simulate the equilibrium with $q_a = 6.794$, as shown in figure 22.

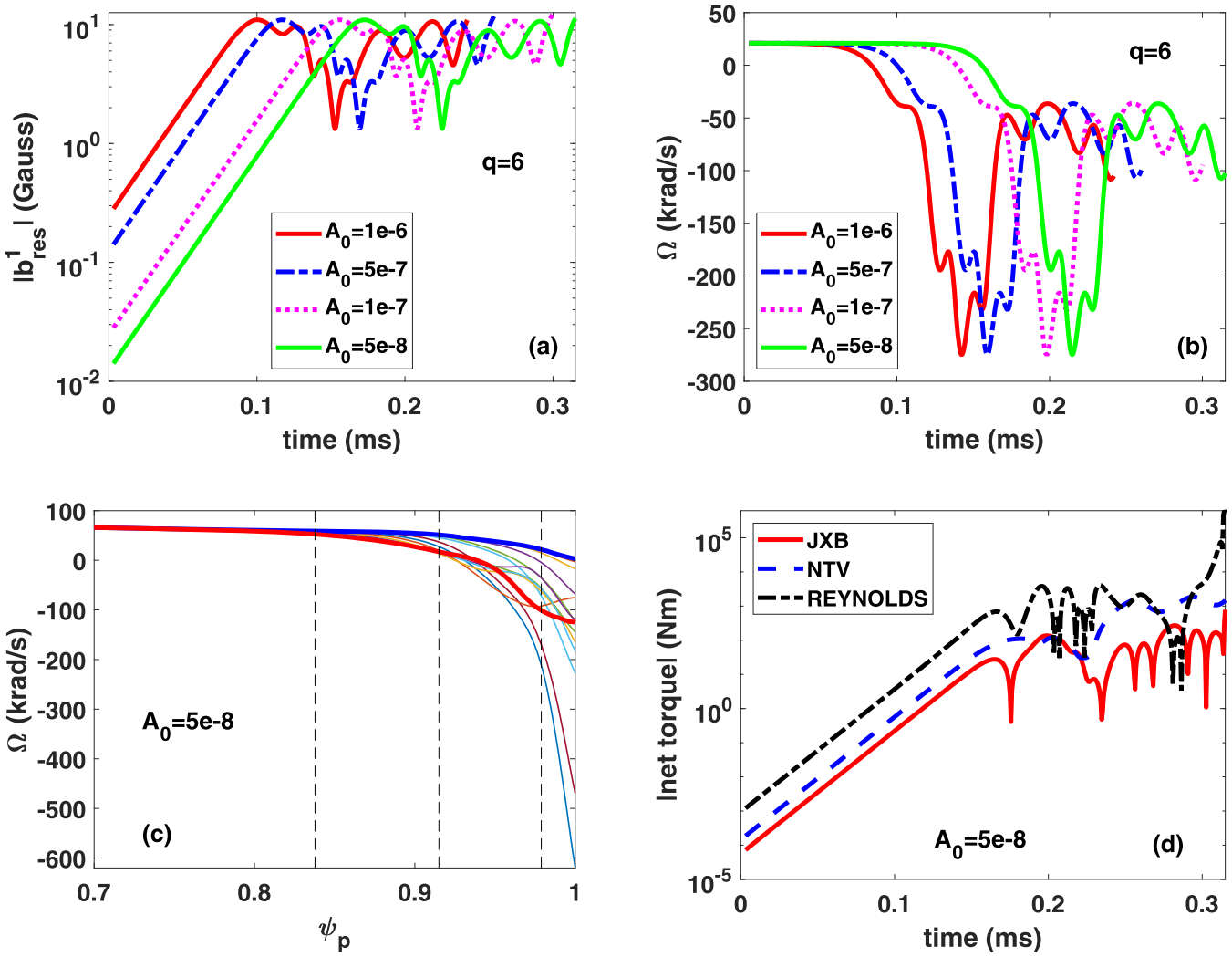

Figure 22. The MARS-Q simulated time traces of the initially unstable $n = 1$ resistive kink-peeling mode: (a) and (b) the perturbed $m/n = 6/1$ resonant radial field component and the toroidal rotation frequency, respectively, at the $q = 6$ rational surface, with different choices for the amplitude A_0 of the initial perturbation; (c) and (d) evolution of the rotation profile and the time traces of three toroidal net torques, respectively, assuming the initial perturbation amplitude of $A_0 = 5 \times 10^{-8}$. The thick blue (red) curve in (c) indicates the initial (final) rotation profile. The vertical dashed lines in (c) indicate locations of the rational surfaces associated with the $n = 1$ perturbation. The initial rotation profile is assumed to be the fluid rotation as shown in figure 1(c). Assumed are the toroidal momentum diffusion coefficient of $\chi_M = 0.1$ m^2 s^{-1}, the resistive wall with the wall time of $\tau_w/\tau_A = 10^4$, the equilibrium with the edge safety factor $q_a = 6.794$, and the Spitzer resistivity for the plasma (with the Lundquist number of $S = 1.867 \times 10^8$).

Again a strong non-linear interaction between the $n = 1$ kink-peeling mode and the plasma flow are simulated. The saturation level for the kink-peeling mode is independent of amplitude of the initial perturbation. The edge flow frequency decreases to a negative value before recovers. Compared to figure 21, the non-linear interaction occurs in an even shorter time scale (sub-milliseconds). This is because the kink-peeling mode is linearly more unstable at $q_a = 6.794$ (figure 5). More unstable mode also drives the plasma edge rotation frequency to a more negative value (figures 22(b) and (c)). The dominant torque contribution is found again to be due to the Reynolds stress (figure 22(d)), although the NTV torque is found to be playing a larger role here, than the case with $q_a = 6.985$.

Flow damping and mode saturation are also simulated for the $n = 2$ mode, as reported by figure 23. Compared to the $n = 1$ mode results reported above, there are two major differences. First, no linearly growing phase of the instability is visible in figure 23(a), showing the time traces of the $m/n = 13/2$ resonant harmonic at the corresponding rational surface. This is because the $n = 2$ mode is linearly marginally unstable within the fluid approximation (figure 5). This leads to a quick non-linear saturation of the mode. The second significant difference is in the toroidal torque evolution (figure 23(d)). The dominant torque contribution for the $n = 2$ mode comes from the NTV torque during the initial phase of simulation. The Reynolds torque takes

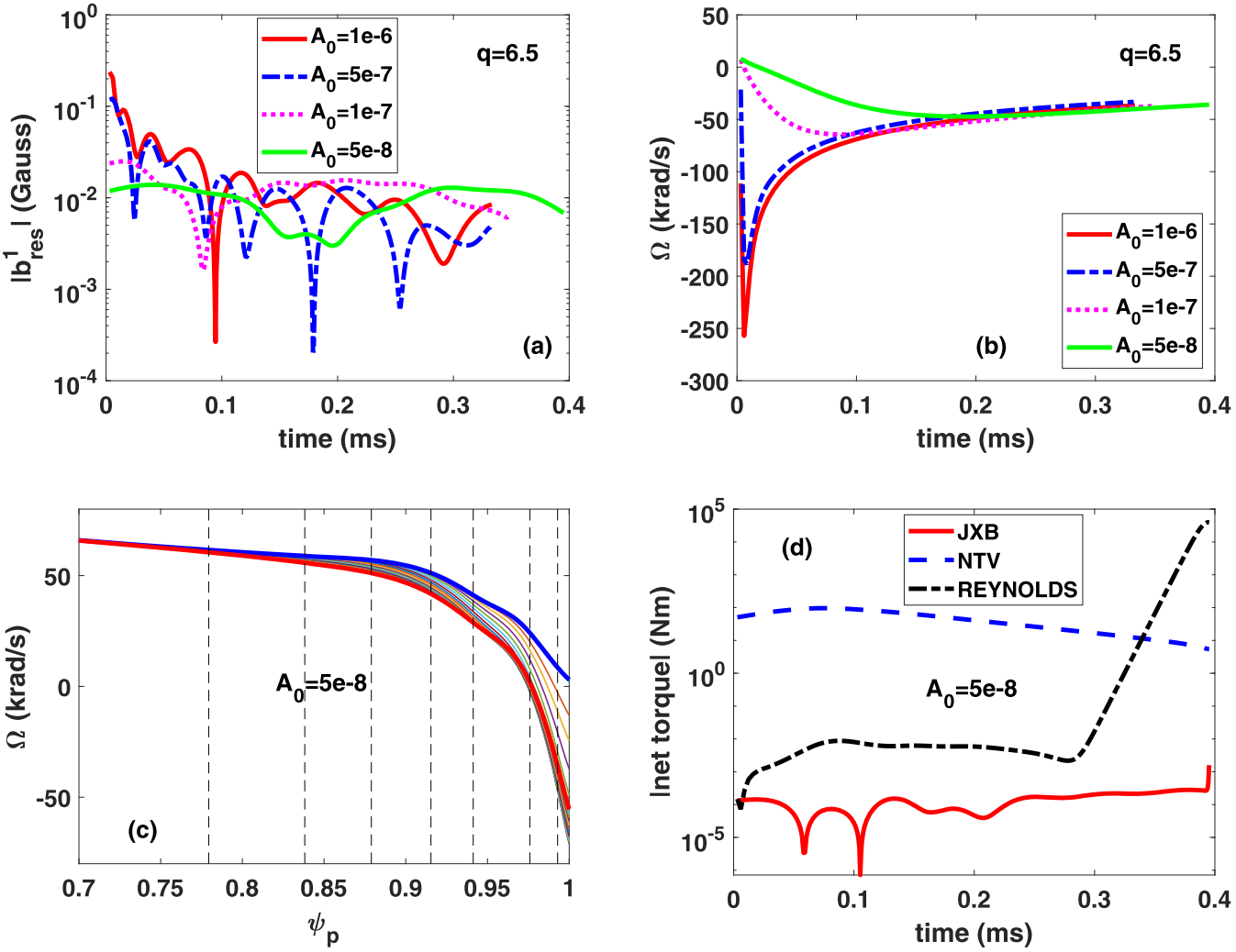

Figure 23. The MARS-Q simulated time traces of the $n = 2$ resistive kink-peeling mode: (a) and (b) the perturbed $m/n = 13/2$ resonant radial field component and the toroidal rotation frequency, respectively, at the $q = 6.5$ rational surface, with different choices for the amplitude A_0 of the initial perturbation; (c) and (d) evolution of the rotation profile and the time traces of three toroidal net torques, respectively, assuming the initial perturbation amplitude of $A_0 = 5 \times 10^{-8}$. The thick blue (red) curve in (c) indicates the initial (final) rotation profile. The vertical dashed lines in (c) indicate locations of the rational surfaces associated with the $n = 1$ perturbation. The initial rotation profile is assumed to be the fluid rotation as shown in figure 1(c). Assumed are the toroidal momentum diffusion coefficient of $\chi_M = 0.1$ m^2 s^{-1}, the resistive wall with the wall time of $\tau_w/\tau_A = 10^4$, the equilibrium with the edge safety factor $q_a = 6.985$, and the Spitzer resistivity for the plasma (with the Lundquist number of $S = 1.867 \times 10^8$).

over only during the later phase of the non-linear interaction between the mode and the plasma flow. With the $n = 1$ perturbation, the Reynolds torque always provides the dominant contribution (figures 21(d) and 22(d)). Finally, we mention that with both the $n = 1$ and $n = 2$ perturbations, no true steady state saturation is achieved during the non-linear interplay phase between the perturbation and the plasma flow. An oscillating behavior is always present.

We emphasize that the quasi-linear model employed in this study does not include the $n = 0$ density and plasma current evolution. In other words, the plasma equilibrium current and density are fixed during the MARS-Q simulations (only the toroidal rotation is allowed to change following equation (9)). Therefore, the saturation that we simulated here comes solely from the flow (and flow shear) effect. It remains a future work to find out whether the RMP induced equilibrium density and current change can further modify the mode saturation as found in reference [13].

6. Summary and discussion

A systematic investigation of the low-n kink-peeling instabilities, and their interaction with the plasma flow, has been carried out based on a QH-mode plasma from the DIII-D discharge 157102. The linear and quasi-linear toroidal modeling has been performed utilizing the MARS-F/K/Q suite of codes.

We find that all the low-n ($n = 1, 2, 3$) modes are strongly localized near the plasma edge. Because of this edge localization, truncation of the plasma separatrix, in other words the edge safety factor q_a, sensitively affects the growth rate of the instability. A systematic scan of the q_a value shows stabilizing effect of the plasma separatrix on these kink-peeling type of instabilities, as expected in theory.

The resistive wall has minor effect on the mode instability, due to the fact that the associated magnetic perturbation decays fast outside the plasma boundary. The plasma resistivity, however, has a strong destabilizing effect on these kink-peeling modes, without significant modification to the mode eigen-structure. The numerically computed mode growth rate is found to scale approximately as $S^{-1/3}$, with S being the Lundquist number.

The plasma toroidal flow, either assuming the fluid flow model or the $E \times B$ flow model, or their linear combination, has relatively weak (stabilizing) effect on these low-n modes. The mode frequency in the laboratory frame is, however, sensitive to the flow model. This is because within the single fluid approximation, these instabilities, with radially highly localized mode structure, tend to rotate together with the plasma. The flow effect on the mode eigen-structure is also not strong, with the $E \times B$ flow inducing more edge localization of the instability.

The drift kinetic effects from thermal particles are found to be strongly destabilizing for these low-n kink-peeling modes. All three types of kinetic resonances, associated with the toroidal precession and bounce motion of trapped particles, as well the transit motion of passing particles, play significant roles in the mode destabilization. This is due to the fact that the instabilities are highly localized in the plasma edge region, where all the particle drift frequencies become small and comparable to the mode frequency (in the plasma frame). Compared to the mode eigenfunction computed within the fluid theory, the non-perturbative MHD-kinetic hybrid model finds modifications of the mode eigen-structure by the drift kinetic effects from thermal particles. The latter essentially push the kink-peeling mode further away from the plasma boundary and toward the pedestal region.

The MARS-F/K computed mode structure is compared to the experimental measurements in DIII-D. The internal perturbation data, i.e. both the plasma temperature and density fluctuations, agree well between the modeling and experiments. The poloidal structure of the external perturbation data, i.e. the magnetic field perturbations measured outside the plasma, also agrees well in both the amplitude and the toroidal phase. Inclusion of the drift kinetic effects slightly improves the agreement for the internal perturbation data but marginally modifies the magnetic perturbation structure outside the plasma.

Finally, the MARS-Q quasi-linear initial value simulations find saturation (with amplitude oscillations) of the kink-peeling instability, due to the non-linear interplay between the low-n perturbation and the plasma toroidal flow. More specifically, we find that the $n = 1$ kink-peeling instability damps the $n = 0$ plasma flow, which in turn stabilizes the $n = 1$ instability. The simulated time for reaching the non-linear interaction stage depends on the (assumed) initial perturbation amplitude, but the typical time scale is within milliseconds. The kink-peeling mode changes both the flow amplitude and flow shear near the plasma edge. According to our modeling, the stabilization and saturation of the kink-peeling mode are due to the combination of both the flow amplitude damping and the slight increase of the flow shear. This reveals one possible physics mechanism of achieving EHOs as observed in experiments. The Reynolds stress torque is found to generally play a major role in the flow damping, though the NTV torque can also play a dominant role in certain cases (e.g. the initial simulation phase of the $n = 2$ perturbation).

We remark that two-fluid effects are largely neglected in this work. Generally speaking, two-fluid effects can modify the kink-peeling instability in particular by introducing the diamagnetic flow. On the other hand, the latter may have limited effects on the instabilities that we studied here, which are strongly localized near the plasma edge. In fact, these low-n modes are located near the pedestal foot where the diamagnetic flow is probably slow (and probably somewhat uncertain too, given the difficulty to accurately measure the density and temperature profiles near the plasma separatrix). With the MARS-K computations, the diamagnetic effect is partially taken into account via the drift kinetic closure (which naturally follows a two-fluid treatment). However, the finite Larmor radius correction to the perturbed momentum equation, which is an important diamagnetic effect associated with two-fluid formulation, is still neglected in the MARS-K computation.

Finally, we point out that our study provides one possible explanation for EHOs. The eventual saturation mechanism may involve multiple physics interactions. Besides, this work only investigates the low-n kink-peeling instabilities as a potential candidate for EHOs. Investigation of higher-n instabilities (and the effect of toroidal flow, plasma resistivity, drift kinetic contribution, etc on these instabilities) in this DIII-D plasma remains a future work.

Disclaimer

Acknowledgments

This work is supported by and the National Magnetic Confinement Fusion Science Program of China under Contact Nos. 2019YFE03010003, 2017YFE0301202 and National Natural Science Foundation of China under Contact Nos. 11775067, 11605046 and 11875018. The work is also supported by US

DoE Office of Science under Contract DE-FG02-95ER54309 and DE-FC02-04ER54698.

ORCID iDs

G.Q. Dong https://orcid.org/0000-0002-4289-4060
Y.Q. Liu https://orcid.org/0000-0002-8192-8411
X. Chen https://orcid.org/0000-0002-8718-6877
G.Z. Hao https://orcid.org/0000-0003-2310-6134
S. Wang https://orcid.org/0000-0001-6480-7004
N. Zhang https://orcid.org/0000-0003-3985-8031

References

[1] Burrell K.H. *et al* 2005 *Phys. Plasmas* **12** 056121
[2] Maingi R. *et al* 2014 *Nucl. Fusion* **54** 114016
[3] Greebfield C.M. *et al* 2001 *Phys. Rev. Lett.* **86** 4544
[4] Burrell K.H. *et al* 2001 *Phys. Plasmas* **8** 2153
[5] Suttrop W. *et al* 2005 *Nucl. Fusion* **45** 721
[6] Sakamoto Y., Shirai H., Fujita T., Ide S., Takizuka T., Oyama N. and Kamada Y. 2004 *Plasma Phys. Control. Fusion* **46** A299
[7] Oyama N. *et al* 2005 *Nucl. Fusion* **45** 871
[8] Burrell K.H. *et al* 2002 *Plasma Phys. Control. Fusion* **44** A253
[9] Suttrop W. *et al* 2003 *Plasma Phys. Control. Fusion* **45** 1399
[10] Snyder P.B. *et al* 2007 *Nucl. Fusion* **47** 961
[11] Wilson H.R., Cowley S.C., Kirk A. and Snyder P.B. 2006 *Plasma Phys. Control. Fusion* **48** A71
[12] Chen X. *et al* 2016 *Nucl. Fusion* **56** 076011
[13] Liu F., Huijsmans G.T.A., Loarte A., Garofalo A.M., Solomon W.M., Snyder P.B., Hoelzl M. and Zeng L. 2015 *Nucl. Fusion* **55** 113002
[14] King J.R., Kruger S.E., Burrell K.H., Chen X., Garofalo A.M., Groebner R.J., Olofsson K.E.J., Pankin A.Y. and Snyder P.B. 2017 *Phys. Plasmas* **24** 055902
[15] Liu F. *et al* 2018 *Plasma Phys. Control. Fusion* **60** 014039
[16] Liu Y., Kirk A. and Sun Y. 2013 *Phys. Plasmas* **20** 042503
[17] Liu Y.Q., Bondeson A., Fransson C.M., Lennartson B. and Breitholtz C. 2000 *Phys. Plasmas* **7** 3681
[18] Liu Y., Chu M.S., Chapman I.T. and Hender T.C. 2008 *Phys. Plasmas* **15** 112503
[19] Xia G., Liu Y., Liu Y., Hao G.Z. and Li L. 2015 *Nucl. Fusion* **55** 093007
[20] Liu Y., Chapman I.T., Graves J.P., Hao G.Z., Wang Z.R., Menard J.E., Okabayashi M., Strait E.J. and Turnbull A. 2014 *Phys. Plasmas* **21** 056105
[21] Dong G.Q., Liu Y.Q., Liu Y., Wang S., Zhang N., Hao G.Z. and Xia G.L. 2019 *Nucl. Fusion* **59** 066011
[22] Shaing K.C., Sabbagh S.A. and Chu M.S. 2010 *Nucl. Fusion* **50** 025022
[23] Sun Y. *et al* 2010 *Plasma Phys. Control. Fusion* **52** 105007
[24] Liu Y., Chu M.S., In Y. and Okabayashi M. 2010 *Phys. Plasmas* **17** 072510
[25] Liu Y., Saarelma S., Gryaznevich M.P., Hender T.C. and Howell D.F. 2010 *Plasma Phys. Control. Fusion* **52** 045011
[26] Webster A.J. and Gimblett C.G. 2009 *Phys. Plasmas* **16** 082502
[27] Dong G.Q., Liu Y.Q., Wang S., Zhang N., Yu D.L., Liu Y. and Wang Z.R. 2017 *Phys. Plasmas* **24** 112510
[28] Strait E.J. *et al* 2006 *Rev. Sci. Instrum.* **77** 023502
[29] Baker D.R. *et al* 1998 *Nucl. Fusion* **38** 485